iScience

CellPress
OPEN ACCESS

Article

# *HIF2A* gain-of-function mutation modulates the stiffness of smooth muscle cells and compromises vascular mechanics

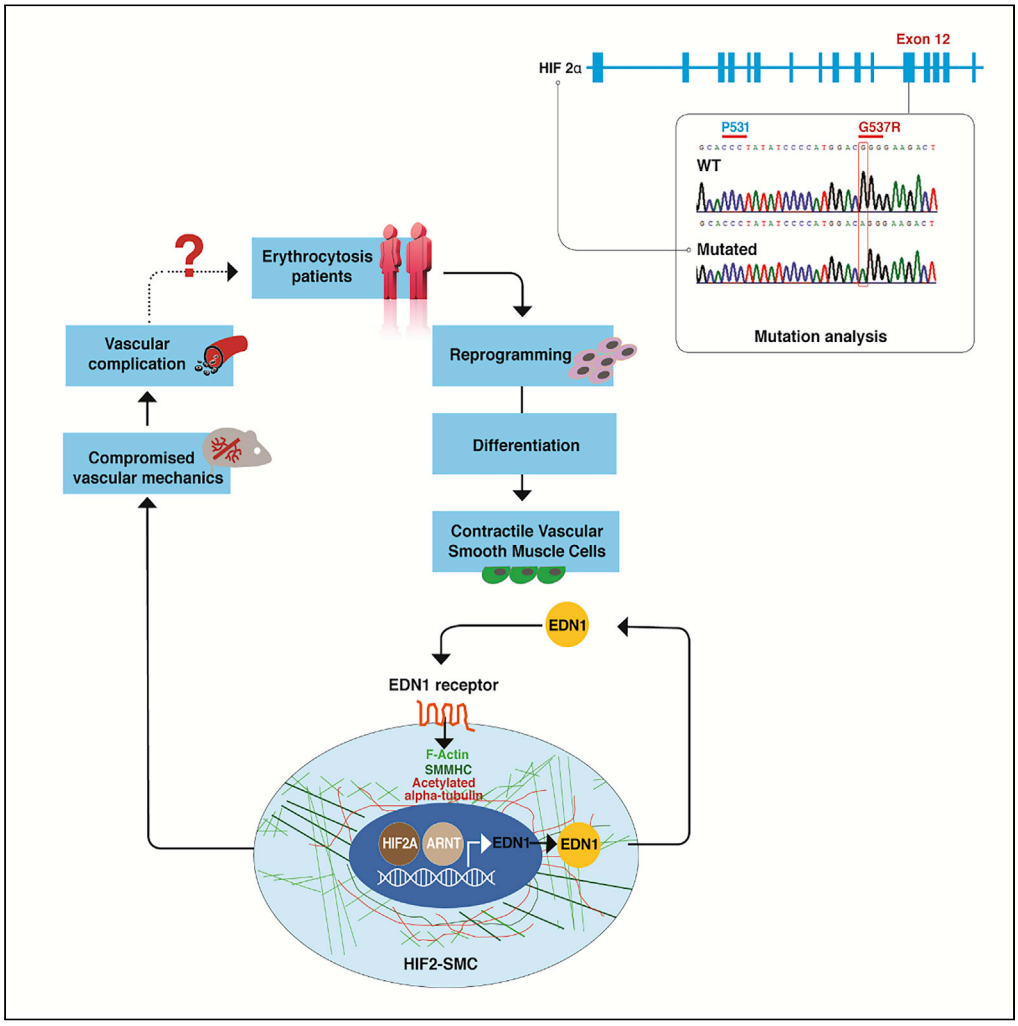


Xin Yi Chan, Eugenia Volkova, Joon Eoh, ..., Frank S. Lee, Josef T. Prchal, Sharon Gerecht

gerecht@jhu.edu

## HIGHLIGHTS

HIF2-SMCs are stiffer than WT-SMCs and differ in contractile SMC marker expression

HIF2-SMCs and WT-SMCs differ in *EDN1* production and ECM composition

HIF- 2α induces *EDN1*; EDNI subsequently induces SMC stiffening

Hif2A GOF mouse arterial SMCs have more disorganized stress fibers and are stiffer

Chan et al., iScience *24*, 102246
April 23, 2021 
https://doi.org/10.1016/j.isci.2021.102246

iScience

CellPress
OPEN ACCESS

Article

# *HIF2A* gain-of-function mutation modulates the stiffness of smooth muscle cells and compromises vascular mechanics

Xin Yi Chan,[1,10] Eugenia Volkova,[1,10] Joon Eoh,[1] Rebecca Black,[1] Lilly Fang,[1] Rayyan Gorashi,[1] Jihyun Song,[2] Jing Wang,[3] Morgan B. Elliott,[1,4] Sebastian F. Barreto-Ortiz,[5] James Chen,[5] Brian L. Lin,[6] Lakshmi Santhanam,[5] Linzhao Cheng,[3] Frank S. Lee,[7] Josef T. Prchal,[2] and Sharon Gerecht[1,4,8,9,11,*]

## SUMMARY

**Heterozygous gain-of-function (GOF) mutations of hypoxia-inducible factor 2α (HIF2A), a key hypoxia-sensing regulator, are associated with erythrocytosis, thrombosis, and vascular complications that account for morbidity and mortality of patients. We demonstrated that the vascular pathology of HIF2A GOF mutations is independent of erythrocytosis. We generated HIF2A GOF-induced pluripotent stem cells (iPSCs) and differentiated them into endothelial cells (ECs) and smooth muscle cells (SMCs). Unexpectedly, HIF2A-SMCs, but not HIF2A-ECs, were phenotypically aberrant, more contractile, stiffer, and overexpressed endothelin 1 (EDN1), myosin heavy chain, elastin, and fibrillin. EDN1 inhibition and knockdown of *EDN1*-receptors both reduced HIF2-SMC stiffness. Hif2A GOF heterozygous mice displayed pulmonary hypertension, had SMCs with more disorganized stress fibers and higher stiffness in their pulmonary arterial smooth muscle cells, and had more deformable pulmonary arteries compared with wild-type mice. Our findings suggest that targeting these vascular aberrations could benefit patients with HIF2A GOF and conditions of augmented hypoxia signaling.**

## INTRODUCTION

Hypoxia-inducible factors (HIF-1 and HIF-2) maintain oxygen homeostasis and control many physiological processes, including angiogenesis and erythropoiesis (Semenza, 2001). HIFs activity is tightly regulated in an oxygen-dependent manner; in normoxia, HIFs-alpha subunits are degraded, whereas in hypoxia HIFs-alpha proteins stabilize, bind to the constitutively expressed beta subunits, and HIFs dimers translocate into the nucleus to activate a broad range of downstream targets (Kaelin and Ratcliffe, 2008; Majmundar et al., 2010). Mutations affecting multiple components in the HIF pathway have been identified as causes for the expansion of red blood cell mass termed "erythrocytosis" or "polycythemia." These mutations include loss-of-function mutations of the two principal HIFs' negative regulators, i.e. prolyl hydroxylase domain protein 2 (PHD2 encoded by *EGLN1*) and von Hippel Lindau (*VHL*) as well as gain-of-function (GOF) mutations in HIF2A (encoded by *EPAS1*). When any one of these proteins are mutated, HIF2A, the principal regulator of erythropoietin (EPO), is stabilized and leads to erythrocytosis (Wenger and Hoogewijs, 2010). Management of erythrocytosis is limited to reducing red blood cells via venesection, which does not ameliorate vascular complications and may even have a detrimental effect on those complications (Sergueeva et al., 2015; Gordeuk et al., 2019). Here we propose that the morbidity and mortality of these rare congenital disorders of HIF-2 upregulation are defined not by their erythroid phenotype but by HIF-2 driven vascular and thrombosis complications.

Previous work has shown that a knock-in mouse model with a GOF missense mutation in *EPAS1*, corresponding to a human-associated erythrocytosis mutation (G537W), exhibits erythrocytosis and pulmonary hypertension (PH) (Tan et al., 2013). Studies in mice also show that accumulation of HIF2A via the deletion of *EGLN1* in ECs is sufficient to cause vascular stiffening independent of erythrocytosis (Kapitsinou et al., 2016b; Dai et al., 2016). Endothelium signaling and interactions with the surrounding smooth muscle cells (SMCs) play a crucial role in regulating vascular function and in mediating vascular tone by generating and maintaining the balance between vasodilators and vasoconstrictors. When the endothelium is

[1]Department of Chemical and Biomolecular Engineering and Institute for NanoBioTechnology, Johns Hopkins University, Baltimore, MD 21218, USA

[2]Hematology, University of Utah School of Medicine and Huntsman Cancer Center, Salt Lake City, UT 84132, USA

[3]Division of Hematology and Institute for Cell Engineering, Johns Hopkins School of Medicine, Baltimore, MD 21205, USA

[4]Department of Biomedical Engineering, Johns Hopkins University School of Medicine, Baltimore, MD 21205, USA

[5]Department of Anesthesiology and Critical Care Medicine, Johns Hopkins University School of Medicine, Baltimore, MD 21205, USA

[6]Division of Cardiology, Johns Hopkins Medical Institutions, Baltimore, MD 21205, USA

[7]Department of Pathology and Laboratory Medicine, Perelman School of Medicine, University of Pennsylvania, 605 Stellar Chance Labs, 422 Curie Boulevard, Philadelphia, PA 19104, USA

[8]Department of Materials Science and Engineering, Johns Hopkins University, Baltimore, MD 21218, USA

[9]Department of Oncology, Johns Hopkins University School of Medicine, Baltimore, MD 21205, USA

[10]These authors contributed equally

[11]Lead contact

*Correspondence: gerecht@jhu.edu

https://doi.org/10.1016/j.isci.2021.102246

A

| Cell Line derived | Sex | Mutation | Clinical Details |
|---|---|---|---|
| WT-hiPSC | Unknown | None | |
| HIF2-hiPSC | F | HIF2A$^{G537R}$ | Elevated hemoglobin at birth. EPO levels repeatedly elevated through lifetime. |
| F-WT-hiPSC | F | None | |
| F-F-HIF2-hiPSCs | F | HIF2A$^{M535V}$ | Stroke at age 21. |
| F-M-HIF2-hiPSCs | M | HIF2A$^{M535V}$ | Myocardial infarction at age 24, two coronary artery occlusions, hepatic vein thrombosis. |

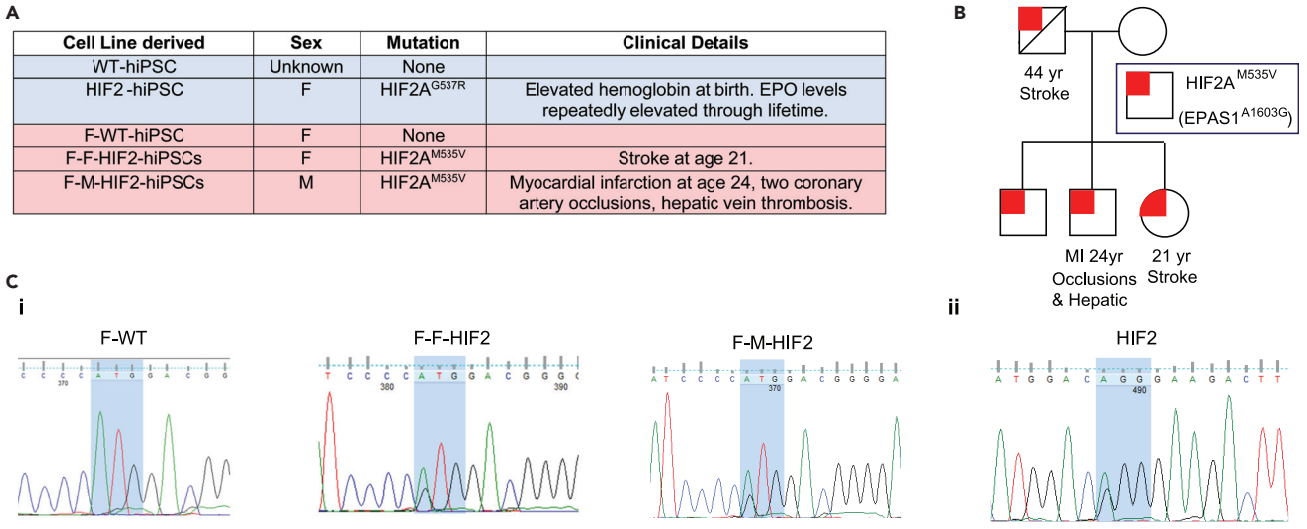


**Figure 1. Generation of hiPSC lines with HIF2A GOF mutation**

(A) Five hiPSC lines were isolated from peripheral blood CD34$^+$ MNCs. Red-filled cells indicate familial lines; blue-filled cells indicate non-familial lines.

(B) The HIF2A$^{M535V}$ (*EPAS1*$^{A1603G}$) mutation family participated in donating peripheral blood CD34$^+$ cells for generating hiPSCs.

(C) Sanger sequencing results show that (1) F-HIF2-hiPSC lines each has a single heterozygous mutation of M535V (*EPAS1*$^{A1603G}$) and (2) the HIF2-hiPSC line has a heterozygous missense mutation of HIF2A$^{G537R}$ (G→ A on exon 12 of *EPAS1* gene).

See also Figures S1 and S2.

dysfunctional, the expression of endothelin 1 (EDN1) increases, causing a decrease in endothelial nitric oxide (NO) production (Iglarz and Clozel, 2007). This altered balance results in a shift toward increased vascular tone due to increased deposition of extracellular matrix (ECM) proteins, as well as hyperplasia and hypertrophy of SMCs. In the pulmonary arteries (PAs), this leads to stiffening, as shown in patients suffering from PH (Furchgott and Vanhoutte, 1989; Cacoub et al., 1997; Ergul et al., 2006). Recently, other studies have suggested that this stiffening of arteries leads to systemic hypertension, which further leads to vessel stiffening everywhere in the body.

The availability of human-induced pluripotent stem cells (hiPSCs) provides a unique approach to interrogate the causes of morbidity and mortality of individuals inheriting HIF2A GOF mutations. These HIF2A GOF (HIF2) hiPSCs allowed us to determine the role of individual cellular vascular components on vascular irregularities in not only ECs but also in SMCs, which dictate the mechanical properties of blood vessels in healthy individuals and patients suffering from vascular and thrombotic complications. Herein, we generated two sets of HIF2 hiPSC lines from the peripheral blood of patients with erythrocytosis caused by HIF2A GOF, differentiated them into ECs and SMCs, and demonstrated that these heterozygous mutations (G537R and M535V) are sufficient to induce cellular alterations in SMCs. We also performed *in vivo* studies using heterozygous mice to further demonstrate early onset of pulmonary hypertension, alterations in SMCs, and compromised vascular mechanics.

## RESULTS

### Patient-specific *HIF2A* missense mutation hiPSC

Five sets of hiPSCs were generated from peripheral blood CD34$^+$ mononuclear cells (MNCs) with the indicated mutations (Figure 1A). Three of the hiPSC cell lines were from a five-generational pedigree with erythrocytosis inherited in an autosomal dominant fashion. This pedigree displayed diverse vascular complications, such as myocardial infarction and stroke, in young individuals (Figure 1B). No other risk factors for cardiovascular morbidity were present. Furthermore, these complications were not prevented by the strict control of their erythrocytosis aimed to reduce hematocrit by regular phlebotomies. We generated the indicated lines from a healthy mother and two offspring.

All these hiPSC lines were found to maintain normal karyotype, expressed pluripotent markers, and underwent differentiation to all three germ layers (Figures S1 and S2). Their genotyping confirmed the mutations

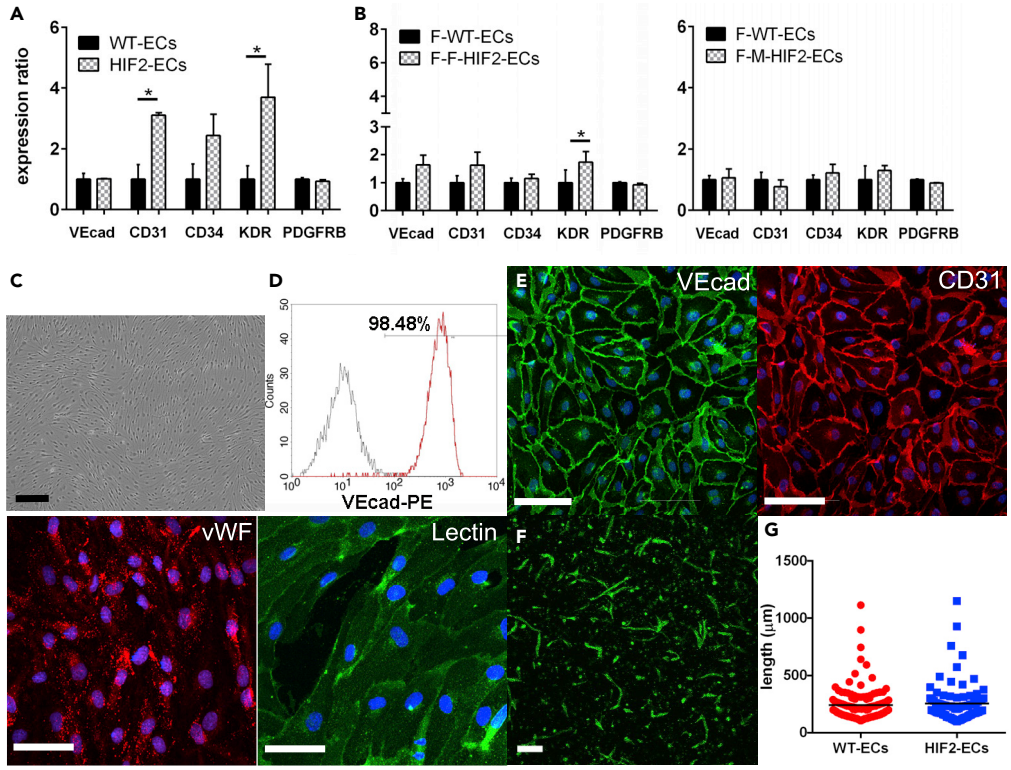


**Figure 2. Maturation of functional HIF2-ECs**

(A and B) Flow cytometry of vascular marker expression on day 6 differentiation of (A) WT-hiPSC versus HIF2-hiPSC and (B) F-WT-hiPSC versus F-HIF2-hiPSC (N = 3).

(C and D) (C) Light microscopy image of sorted VEcad$^+$ cells. Scale bar is 200 μm. (D) Representative flow cytometry histogram for VEcad expression of magnetically sorted VEcad$^+$ cells (N = 4).

(E) Representative immunofluorescence (IF) images of VEcad, CD31, vWF, and binding of *Ulex europaeus* lectin. Images are shown for ECs derived from HIF2-hiPSCs. Nuclei in blue. Scale bars are 100 um.

(F) 3-dimensional vascular networks of HIF2-ECs in collagen I gels. Scale bar is 200 μm.

(G) Length of 3D networks in WT-ECs and HIF2-ECs (N = 3). Data are represented as individual EC networks (points) and mean (black line). Significance level is set at *$p < 0.05$ for a two-tailed t test.

found in the native cells of these individuals (Figure 1B). Similar to other cases of erythrocytosis-associated *EPAS1* mutations, these mutations (G537R and M535V) affect a residue C-terminal to the LXXLAP motif (where underlining indicates the site of hydroxylation). Mutations in residue C-terminal to the LXXLAP motif have been shown to result in impaired degradation and abnormal stabilization of HIF2A (Furlow et al., 2009).

## Endothelial cell differentiation and maturation from HIF2-hiPSCs

We first examined whether HIF2-hiPSCs have a similar vascular differentiation potential as the WT-hiPSC. We used a feeder-free protocol adapted from Lian et al. (Lian et al., 2014; Chan et al., 2015; Smith et al., 2017) (Figure S3A) to derive early vascular cells (EVCs), a bicellular population that includes both vascular endothelial cadherin (VEcad)$^+$ early ECs and platelet-derived growth factor receptor beta (PDGFR)$^+$ support cells (Chan et al., 2015; Kusuma et al., 2013). On day 6 of EC differentiation, HIF2-hiPSCs and F-F-HIF2-hiPSCS generated a higher percentage of kinase insert domain receptor (KDR)$^+$ cells, and HIF2-hiPSCs also generated a higher percentage of CD31$^+$ cells. F-F-HIF2-hiPSCs also exhibited a trend toward a higher percentage of CD31$^+$ cells; however, this was not statistically significant (Figures 2A and 2B). Day 8 EVCs contained cobblestone-like clusters, suggestive of an endothelial-like morphology (Figure S3B). HIF2-hiPSC-derived EVCs contain both early ECs positive for VEcad at intercellular junctions and early pericytes positive for PDGFRβ (Figure S3C). Overall, we found that HIF2- and F-HIF2-hiPSCs have a similar efficiency in EC derivation when compared with the WT- and F-WT-hiPSC lines (Figures S3D–S3F). When embedded in 3D Collagen I gel, the EVCs self-assembled and formed networks (Figure S3G).

Following successful EVC differentiation from HIF2-hiPSC, we examined endothelial maturation and functionality of the HIF2-hiPSC- and F-HIF2-hiPSC-derived ECs (hereafter, abbreviated to HIF2-ECs and F-HIF2-ECs). VEcad$^+$ early ECs were sorted and expanded for four additional passages (Kusuma et al., 2013, 2015), in which they maintained their cobblestone morphology as typical ECs (Figure 2C). These sorted and cultured ECs were verified to have at least 98% VEcad$^+$ cells (Figure 2D). HIF2-ECs had membrane expression of VEcad and CD31, as well as cytoplasmic punctate expression of von Willebrand factor (vWF). These HIF2-ECs also demonstrated the ability to bind to lectin *Ulex europaeus* (Figure 2E). Altogether, HIF2- and F-HIF2-ECs exhibited mature endothelial characteristics comparable to ECs derived from WT- and F-WT-hiPSCs (Kusuma et al., 2013; Chan et al., 2015) (hereafter, abbreviated to WT-ECs and F-WT-ECs). When embedded in collagen I gels, HIF2-ECs self-assembled to form luminal vascular networks at a similar capacity as WT-ECs (Figures 2F and 2G).

## The HIF2A heterozygous mutation affects the expression of vasodilators and vasoconstrictors in HIF2-ECs

A single missense mutation located near the hydroxylation site, Pro-531, can interfere with the hydroxylation of HIF2A and lead to its accumulation under atmospheric conditions *in vitro* (Furlow et al., 2009; Lee and Percy, 2011). We began by examining whether HIF2A accumulation could be observed in HIF2-ECs generated from a patient with a heterozygous mutation near the HIF2A proline hydroxylation. Comparing the expression level of HIF2A in HIF2-ECs and WT-ECs cultured in atmospheric (21% oxygen) and hypoxic (1.0% oxygen) conditions, we observed higher levels of HIF2A expression in HIF2-ECs in comparison to WT-ECs under atmospheric conditions (Figure 3A). Under hypoxic conditions, both HIF2-ECs and WT-ECs expressed higher level of HIF2A.

We then found that *HIF1A* and *HIF2A* were transcribed at similar levels throughout all cell lines (Figures 3B, 3C, and S4). Next, we examined if mRNA expression levels of vasodilators and vasoconstrictors were affected by this *HIF2A* missense mutation. We found that relative expression levels of nitric oxide synthase 2 (*NOS2*), which encodes for a cytokine-inducible NOS, is comparable in both control and HIF2-ECs (Figure 3D). Expression of nitric oxide synthase 3 (*NOS3*), which encodes endothelial nitric oxide synthase (eNOS), was similar or lower in HIF2-mutated ECs when compared with WT-ECs (Figures 3E and S4). Downregulation of *NOS3* was further verified in immunostaining of eNOS in which the intensity of labeling was lower in HIF2-ECs when compared with WT-ECs (Figure 3F). In hypoxia, *HIF2A* is reported to regulate apelin (APLN), a vasodilatory peptide acting by binding to the apelin G-protein-coupled receptor (APLNR) (Kapitsinou et al., 2016b). Here, we found lower *APLN* and *APLNR* expression in HIF2-ECs when compared with WT-ECs (Figure 3G), and similar or lower expression levels in F-WT-ECs and F-M-HIF2-ECs (Figure S4). We then examined the expression level of Arginase 1, an NO inhibitor downstream of HIF-2$\alpha$ but could detect its transcript in neither HIF2 nor WT-ECs (Berkowitz et al., 2003; Dai et al., 2016). Next, we examined the *EDN1* transcript, a potent vasoconstrictor implicated in the pathogenesis of PH. We found higher expression of *EDN1* in both HIF2-ECs and F-HIF2-ECs compared with their WT-EC controls (Figures 3I and S4A) but with similar levels of EDN1 secretion between WT-ECs and HIF2-ECs (Figure 3I). Finally, atomic force microscopy (AFM) measurements revealed that HIF2-ECs were stiffer than WT-ECs (Figure 3K).

## Smooth muscle cell differentiation and maturation from HIF2-hiPSCs

Previous studies show that ECs are the primary source for EDN1 generation, but a recent study has demonstrated that EDN1 generated by SMCs may independently modulate vascular tone (Kim et al., 2015). We investigated whether the *HIF2A* mutation had a detrimental effect on hiPSC-derived SMCs alone (Vo et al., 2010; Wanjare et al., 2013). We followed an established differentiation protocol to generate mature smooth muscle-like cells (mSMLC) and then further matured them into contractile SMCs (Wanjare et al., 2013, 2014). Features of the mSMLCs derived from HIF2-hiPSCs included irregular morphologies, hypertrophy, increased stress fibers, and upregulation of smooth muscle myosin heavy chain (SMMHC and *MYHCII*) and EDN1 when compared with mSMLCs derived from WT-hiPSCs (Figures S5A–S5E). When comparing contractile SMCs derived from WT-hiPSCs (hereafter, WT-SMCs) and HIF2-SMCs, as well as, F-WT- and F-HIF2-SMCs, we noticed that HIF2-SMCs (derived from UT2HIF2A-hiPSC line) lacked the typical elongated, spindle-shaped phenotype of contractile SMCs. Instead, HIF2-mutated SMCs exhibited hypertrophy, jagged borders, and excessive amounts of actin stress fibers and acetylated alpha-tubulin (Figures 4A and S6A). The arrangements of F-actin filaments were randomly aligned in HIF2-SMCs but appeared to be more organized and aligned in WT-SMCs. When compared with WT-SMCs, HIF2-SMCs not only express SMMHC at a higher level (Figures 4A and 4B) but also have an increased prevalence of F-actin stress

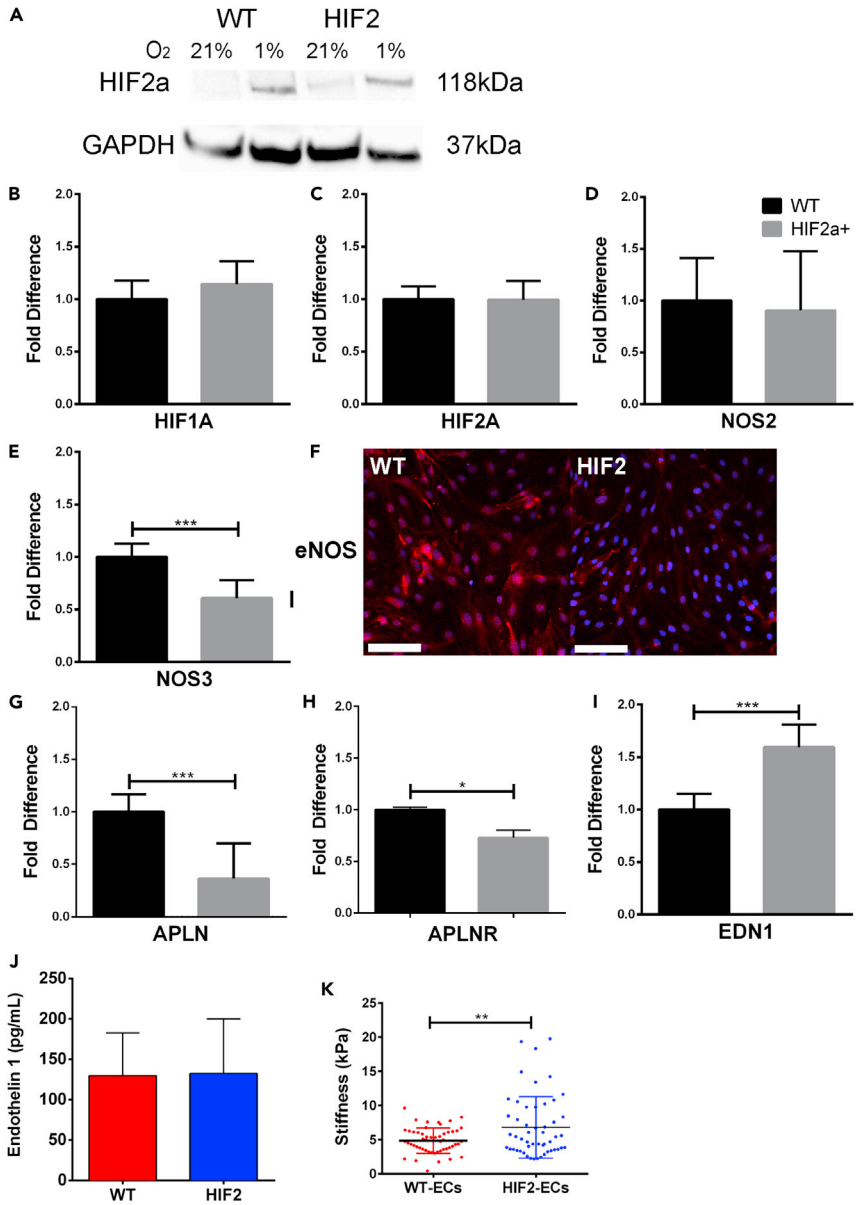


**Figure 3. HIF2A-mutation-induced differences in vasoconstrictor and vasodilators in HIF2-ECs**

(A) Representative western blot of HIF2A for HIF2-ECs and WT-ECs.

(B–E; G–I) qRT-PCR of HIF2-ECs. Data are presented as the fold-change difference in reference to WT-ECs. Expression levels were normalized to endogenous control *GAPDH* expression level (N = 4).

(F) Representative IF images of eNOS stains of WT-ECs and HIF2-ECs (N = 4). Scale bars are 100 μm.

(J) Quantification of EDN1 level in WT-ECs and HIF2-ECs using ELISA (N = 3).

(K) Atomic force microscopy (AFM) analysis of WT-ECs (n = 52) and HIF2-ECs (n = 52) (N = 3). All data are represented as mean ± standard deviation. AFM data is also represented as individual cell measurements. Significance level is set at ***p < 0.001, **p < 0.01, and *p < 0.05 for a two-tailed t test.

See also Figures S3, S4, and S6.

fibers, smooth muscle actin (SMA), and acetylated alpha-tubulin (Figures 4A–4D). Furthermore, EDN1 secretion levels were higher in HIF2-SMCs when compared with WT-SMCs and in F-HIF2-SMCs in comparison to F-WT-SMCs (Figures 4E, 4F, and S6B). Of note, baseline EDN1 concentration was higher in SMCs generated from the family member cell lines when compared with the non-familial cell lines (Figures S4A, S5E, and S6B). Overall, we found qualitative and quantitative phenotypic differences of HIF2-SMCs

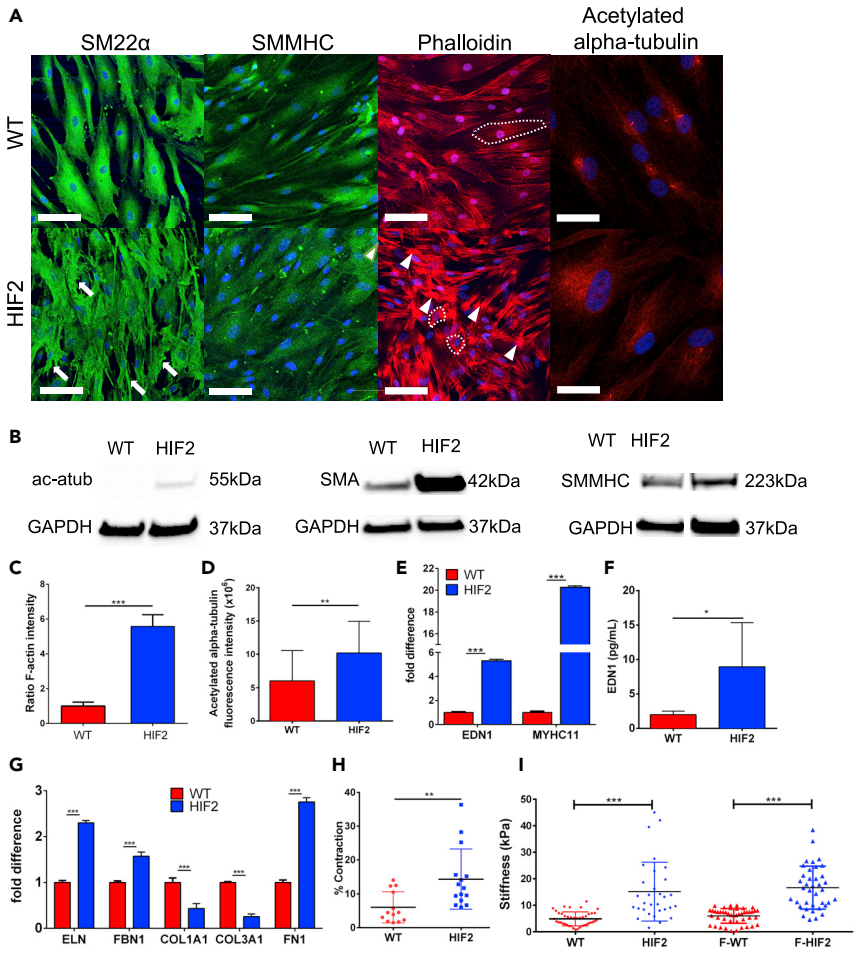


**Figure 4. HIF2-SMCs have abnormal phenotype and changes in ECM deposition compared with WT-SMCs**

(A) Representative IF images of SM22a, SMMHC, phalloidin, and acetylated alpha-tubulin staining. White arrows: jagged border; white arrowheads: dense actin fibers; white dotted lines: examples of isotropic fiber arrangement in WT-SMCs and anisotropic fiber arrangement in HIF2-SMCs. Scale bars are 100 μm and 50 μm for acetylated alpha-tubulin.

(B) Representative western blots of acetylated alpha-tubulin, SMA, and SMMHC.

(C and D) Quantification of (C) F-Actin and (D) acetylated alpha-tubulin (N = 4).

(E) qRT-PCR of *EDN1* and *MYHCII*.

(F) Quantification of EDN1 level in WT-SMCs and HIF2-SMCs using ELISA (N = 5).

(G) qRT-PCR of ECM genes. All qPCR data are presented as the fold-change difference in reference to WT-SMCs. Expression levels were normalized to endogenous control of *GAPDH* expression level (N = 4)

(H) Percent contraction upon carbachol treatment (N = 3).

(I) AFM analysis of WT-SMCs (n = 41) and HIF2-SMCs (n = 31); F-WT-SMCs (n = 45) and F-HIF2-SMCs (n = 38) (N = 3). Data are represented as mean ± standard deviation. Data in H and I are also represented as individual cell measurements. Significance level is set at ***p < 0.001, **p < 0.01, and *p < 0.05 for a two-tailed t test.

See also Figures S6–S8.

in both early and mature contractile forms. This suggests that the mutation may have a direct effect in both the early stage and terminally differentiated SMCs.

## Increased stiffness in HIF2-SMCs

Increased expression and accumulation of ECM proteins represent one of the main pathobiological aspects of PH (Tuder et al., 2007). We observed significant changes in elastic ECM expression for HIF2-SMCs when compared with WT-SMCs. HIF2-SMCs consistently express higher transcript levels of the elastic fiber components elastin (*ELN*) and fibrillin-1 (*FBN1*), as well as fibronectin (*FN1*), and lower expression levels of collagen (COL1A1 and *COL3A1*) than WT-SMCs (Figure 4G). A similar observation was made

in mSMLCs (Figure S5F). In correlation with the change in transcript level, ECM expression of elastin, fibrillin-1, and fibronectin are strongly increased in the SMLCs and SMCs derived from HIF2-hiPSCs when compared with their WT counterparts (Figure S7). Contractility, in response to carbachol treatment, individual cell stiffnesses measured via AFM were higher in HIF2-mutated SMCs when compared with SMCs derived from WT (Figures 4H, 4I, and S8). Altogether, these observations suggest that the *HIF2A* mutation in SMCs recapitulates the physiological and pathological observations made in vascular SMCs in PH-related vascular stiffening (Lee et al., 1998).

## EDN1 modulates HIF2-SMC stiffness

To determine whether the SMC phenotype is regulated through HIF2A activation of EDN1, we first knocked down *HIF2A* using siRNA to examine if *EDN1* levels would be reduced. Four days of post-siRNA treatment, *HIF2A* and *EDN1* transcripts were significantly reduced. EDN1 secretion also decreased by more than 2-fold (Figures 5A, 5B, and S9A). We investigated whether these changes would affect cytoskeletal components in knockdown-HIF2-SMCs, but no significant changes were observed in phalloidin and SMMHC expression (Figure S9B). We specifically blocked EDN1 signaling through Bosentan, an antagonist of EDN1 receptors A and B ($ET_A$ and $ET_B$) (Bohm and Pernow, 2007), to investigate whether or not the diseased phenotype of HIF2-SMCs could be diminished by reduction of EDN1 signaling and its downstream targets. Transcript levels of *EDN1* were not affected, as Bosentan inhibits EDN1 binding rather than synthesis. We observed a decrease in the *APLN* transcript, which may have been due to reduced EDN1 signaling (Figure 5C). Both *MYHCII* and *ELN* transcripts were reduced post-Bosentan treatment (Figure 5C). EDN1 is known to regulate vascular tone via cytoskeleton components and secretion of ECMs. At the microtubule level, we noticed that Bosentan-treated HIF2-SMCs had less acetylated alpha-tubulin (stabilized microtubules) in the cytoplasm (Figures 5D and 5E). ECM expression of both the DMSO- and Bosentan-treated HIF2-SMCs was also studied and found to be reduced in treated HIF2-SMCs (Figure S10). After 6 days of 10 μM Bosentan treatment, the stiffness of HIF2-SMCs was significantly reduced in comparison to DMSO-treated controls, likely due to reduced expression of cytoskeletal components, as observed in Bosentan-treated HIF2-SMCs, and further confirmed in *HIF2A* siRNA knockdown HIF2-SMCs (Figures 5F, 5G and S11). In order to reduce the possibility of any non-specific effects of Bosentan, both HIF2- and WT-SMCs were also treated with siRNA to knockdown $ET_A$ and $ET_B$. To better model the effects of the drug, a 2:1 ratio $ET_A$ to $ET_B$ siRNA was chosen. We found similar decreasing trends in transcript levels of *EDN1, APLN*, and *MYHCII* but an increase in *ELN* (Figure 5H). This increase could be due to the ratio of siRNA chosen. Altogether, our findings demonstrate that the *HIF2A* GOF mutation affects downstream EDN1 secretion and signaling, which in turn increases cell stiffness via recruitment and regulation of cytoskeletal proteins.

## Effects of HIF2A mutation on co-culture of hiPSC-ECs and SMCs

After characterizing the HIF2-ECs and HIF2-SMCs individually, we sought to investigate interactions between the mutated cell types through various co-culture model combinations. Because ECs and SMCs constantly interact and regulate vasodilation and vasoconstriction in maintaining vascular homeostasis (Mas, 2009; Sandoo et al., 2010), we wanted to examine whether an additive effect of the mutation was observed in HIF2-SMCs by the HIF2-EC-SMC co-cultures. For these experiments, the WT-SMC-only culture was designated as the experimental control (Figure S12A). When WT-SMCs were co-cultured with WT-ECs, there was a slight decrease in the level of EDN1 in WT-SMCs compared with WT-SMCs cultured alone, suggesting a regulatory effect for the ECs. This same regulatory effect was observed in HIF2-SMCs co-cultured with WT-ECs, in which the EDN1 expression was decreased by 25 percent when compared with HIF2-SMCs cultured alone. In co-cultures with HIF2-ECs, EDN1 in HIF2-SMCs increased by 25%, correlating to the imbalanced levels of vasodilators and vasoconstrictors characteristic of dysfunctional vessels (Figure S12B).

We then examined secreted EDN1 concentrations. We compared the secreted EDN1 concentration of co-culture combinations of WT-SMCs or HIF2-SMCs. We found that WT-SMCs cultured with either WT-ECs or HIF2-ECs secreted EDN1 at similar concentrations (Figure S12C). The same observations were made for HIF2-SMCs cultured with WT-ECs or HIF2-ECs. These results suggest that SMCs play a regulatory role in EDN1 availability in which the HIF2A mutation is responsible for increased EDN1 expression and secretion as shown with the higher secreted EDN-1 levels in both HIF2-SMCs + HIF2-ECs and HIF2-SMCs + WT-ECs co-culture combinations. Overall, the co-culture system conveys a unique perspective in that EDN1 secretion is regulated predominantly by the condition of the SMCs, and co-culturing with healthy ECs is not sufficient for mitigating the effects of the HIF2A mutation.

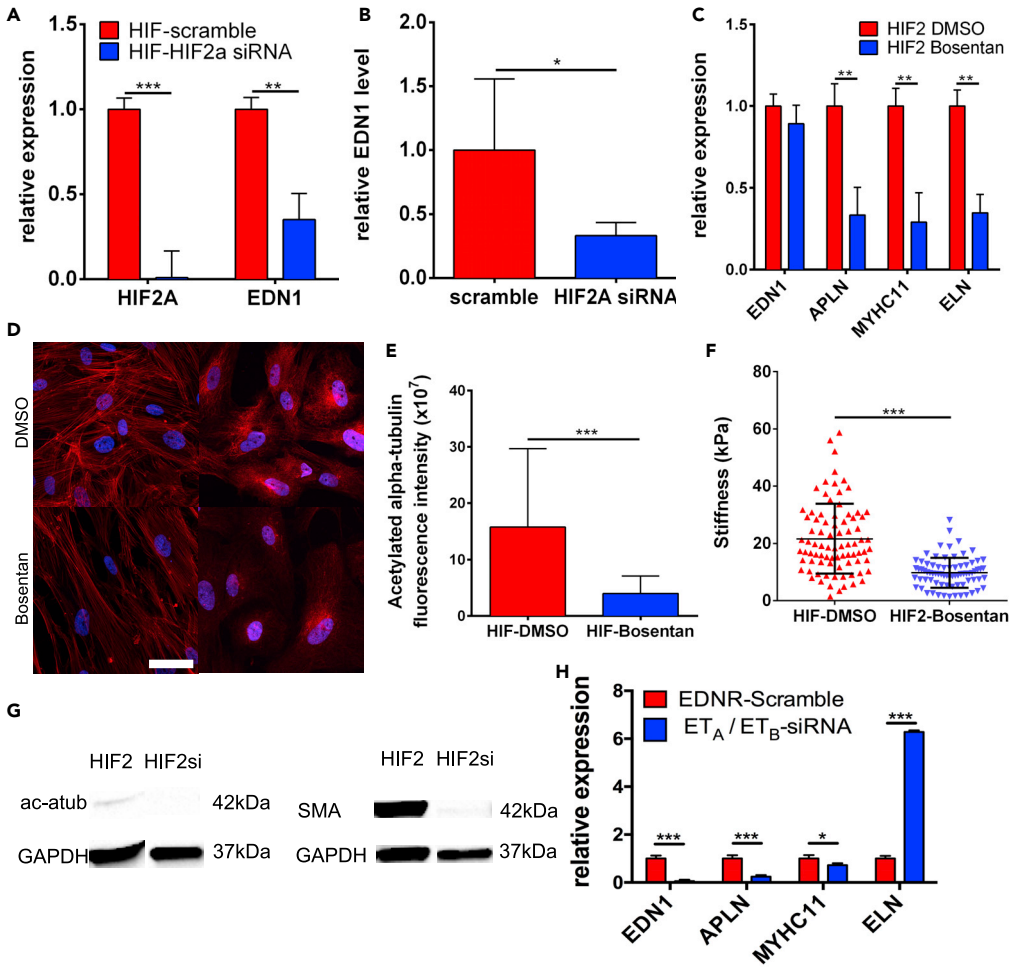


**Figure 5. Upregulated EDN1 modulates HIF2-SMC stiffness**

(A) Level of *HIF2A* and *EDN1* transcripts after siRNA knockdown of HIF2A (N = 3).

(B) EDN1 secretion in control and *HIF2A* siRNA knockdown HIF2-SMCs (N = 5).

(C) qRT-PCR of *EDN1*, *APLN*, *MYHCII*, and *ELN* transcripts in DMSO control and Bosentan-treated HIF2-SMCs (N = 3).

(D) Representative IF images of cytoskeletal protein expression of DMSO control and Bosentan-treated HIF2-SMCs. Scale bar is 50 μm.

(E) Corrected fluorescence intensity of acetylated alpha-tubulin stain in DMSO-treated HIF2-SMC control and Bosentan-treated HIF2-SMC (N = 4).

(F) AFM analysis of DMSO and Bosentan-treated HIF2-SMCs (n = 83 and n = 76, respectively; N = 3).

(G) Representative western blot of acetylated alpha-tubulin and SMA post *HIF2A* siRNA treatment on HIF2-SMCs.

(H) qRT-PCR of *EDN1*, *APLN*, *MYHCII*, and *ELN* expression in HIF2-SMCs after siRNA knockdown of $ET_A$ and $ET_B$ (N = 3).

All data are represented as mean ± standard deviation. Data in F are also represented as individual cell measurements. Significance level is set at ***$p < 0.001$, **$p < 0.01$, and *$p < 0.05$ for a two-tailed t test.

See also Figures S9 and S10.

## HIF2A GOF mutation causes pulmonary hypertension in mice

Because *HIF2A* mutation affects hiPSC-derived SMC properties, we furthered our investigation to heterozygous *Hif2a* G536W knock-in mice (*Hif2a*) and compared them with their WT counterparts (Tan et al., 2013). First, we determined whether HIF2A GOF mutation causes pulmonary hypertension in young mice (Figure 6A). We evaluated right heart function using cardiac catherization to obtain pressure-volume (PV) loops (Figures 6A and 6B). Heart rates were similar across both cohorts. Significant increases in right ventricular pressures ($RVP_{max}$, $RVP_{es}$, SBP, $P_{as}$, $P_{ad}$) were noted in the young HIF2A GOF mutant mice and confirmed pulmonary hypertension. An increase in contractility ($dP/dt_{max}$, PRSW) and relaxation ($dP/dt_{min}$) also demonstrated an apparent impairment in right heart function.

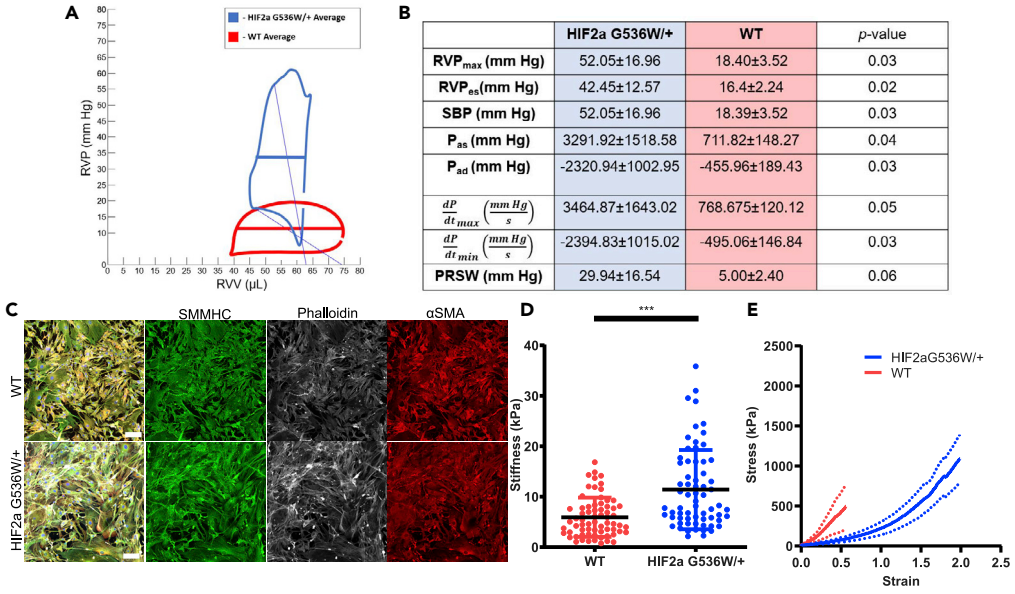


| | HIF2a G536W/+ | WT | *p*-value |
|---|---|---|---|
| $RVP_{max}$ (mm Hg) | 52.05±16.96 | 18.40±3.52 | 0.03 |
| $RVP_{es}$(mm Hg) | 42.45±12.57 | 16.4±2.24 | 0.02 |
| SBP (mm Hg) | 52.05±16.96 | 18.39±3.52 | 0.03 |
| $P_{as}$ (mm Hg) | 3291.92±1518.58 | 711.82±148.27 | 0.04 |
| $P_{ad}$ (mm Hg) | -2320.94±1002.95 | -455.96±189.43 | 0.03 |
| $\frac{dP}{dt_{max}}\left(\frac{mm\,Hg}{s}\right)$ | 3464.87±1643.02 | 768.675±120.12 | 0.05 |
| $\frac{dP}{dt_{min}}\left(\frac{mm\,Hg}{s}\right)$ | -2394.83±1015.02 | -495.06±146.84 | 0.03 |
| PRSW (mm Hg) | 29.94±16.54 | 5.00±2.40 | 0.06 |

**Figure 6. Pulmonary arterial vessels and SMCs in HIF2a$^{G536W/+}$ mice**

(A and B) (A) Average PV loops for a representative *HIF2a*$^{G536W/+}$ mouse compared with a C57/BL6 control. (B) A comparison of *HIF2a*$^{G536W/+}$ mice (blue) and their WT counterparts (red), N = 3, confirms pulmonary hypertension. The right column shows the results of a student's t test.

(C) IF images of SMMHC, phalloidin, and αSMA staining. Scale bars are 100 μm.

(D) AFM analysis of SMCs isolated from pulmonary arteries of *HIF2a*$^{G536W/+}$mice compared with C57/BL6 controls (n = 66; N = 3, and n = 68; N = 3, respectively—each N is a pool from 2 animals). Data is represented as mean ± standard deviation and as individual cell measurements.

(E) Circumferential tensile testing of the mPA from *HIF2a*$^{G536W/+}$ (N = 6) and C57/BL6 age-matched control mice (N = 6). The solid line represents the mean, and the dotted line represents standard deviation. Significance level is set at ***p < 0.001 for a two-tailed t test.

We next sought to examine whether these mice had any alteration in the function of the main pulmonary (mPA), SMCs, and vascular mechanics. Similarly to iPSC-derived HIF2-mutated SMCs, SMCs isolated from the pulmonary arteries of *Hif2a* mice exhibited jagged borders and excessive amounts of disordered actin stress fibers (Figure 6C). They were also significantly stiffer than their WT counterparts when measured via AFM (Figure 6D). As it was vital to obtain functional *in vivo* artery assessment, we next examined the response of the mPA under tensile stress. We focused on the mPA response to stress and found that the *Hif2a* mice have pulmonary arteries that are significantly more deformable when compared with WT mice, suggesting their compromised ability to adequately respond to repetitive physiological stress (Figure 6E).

Next, we attempted to determine the mechanism responsible for the differences in tissue-level and cellular-level mechanical properties (Figure S13). We assessed whether the mRNA expression levels of major ECM components—ELN, collagen 1 (Col1a1), collagen 3 (Col3a1), Fbn1, fibulin4 (Fbln4), and fibulin5 (Fbln5)—and cytoskeletal motor protein MYHCII differed between the lungs of *Hif2a* mice and their wild-type counterparts (Figure S13A). We found no statistically significant differences. Then we examined mRNA expression levels of major remodeling enzymes—metalloproteases-2, -9, and -14 (MMP2, -9, -14)—and found no difference between the two groups (Figure S13B). However, we discovered significant differences in the endogenous ratio of ELN with respect to Col3a1 (ELN/Col3a1) and in the endogenous ratio of Col1a1 with respect to Col3a1 (Col1a1/Col3a1), with the *Hif2a* lungs having higher ratios in both cases (Figure S13C). To assess whether these differences in endogenous ratios—ELN/Col3a1 and Col1a1/Col3a1—translated to the tissue-level scale, we performed histological staining and quantification on mPAs and lung sections. We completed hematoxylin & eosin (H&E), Masson's trichrome stain (MAS), and Verhoeff–Van Giesson (VVG) staining and quantified the medial layer of the vessels for % collagen, % elastin, % total ECM, collagen/elastin ratio, and total area for both mPA and lungs, all of which showed no statistically significant differences (Figures S13D and S13E). However, higher magnification examination of the VVG

staining indicated that elastin banding in the *Hif2a* exhibited a much more heterogeneous morphology (Figures S13Fi–S13Fiii). Although the visual heterogeneity of the elastin bands for *Hif2a* mice was apparent (Figures S13Fii and S13Fiii), further quantification of the number of elastin breaks, elastin branch points, total lamellae, lamellar thickness, and interlamellar distance did not identify a singular tissue-level elastin parameter that clearly differed between the *Hif2a* mice and their wild-type counterparts (Figures S13Fiv–S13Fviii).

## DISCUSSION

Studies using mice and *in vitro* EC cultures have demonstrated that HIF-2α, not HIF-1α, is the key transcription factor responsible for the pathogenesis of PH (Kapitsinou et al., 2016b; Dai et al., 2016). Upon successful differentiation of HIF2-ECs, we examined these cells for mature marker expression, performed functional analyses, and investigated levels of vasoactive components. Although morphologically and functionally HIF2-ECs were not as significantly different when compared with WT-ECs, HIF2-ECs were found to be stiffer when measured via AFM. We observed a slight increase at the *EDN1* transcript level, which did not result in significant differences in the EDN1 secretion levels. A plausible explanation is that the accumulation of HIF-2α under normoxic conditions is not significant enough to exert an effect on the ECs. We observed variability in the expression of *KDR, CD31, NOS3, APLN*, and *APLNR* across our HIF2-EC lines. One potential cause for the EC-heterogeneity is the difference between macrovascular and microvascular ECs. Perhaps ECs of the larger arterial and venous origins are more sensitive to slight changes in HIF-2α levels due to the direct effect of vascular stiffening on these structures, unlike microvascular ECs that are affected at later stages of the disease and are more similar to HIF2-ECs. Another cause may be the differing environmental factors in the lives of the donors.

We then analyzed another critical component of the macrovasculature, the SMCs. We successfully differentiated patient-specific HIF2-iPSCs into mSMLCs and contractile SMCs. In the early stages of SMC differentiation, we were able to detect a noticeable difference between WT and HIF2-mSMLCs in terms of cell size and morphology. This was demonstrated by the presence of dense actin fibers and an irregular rhomboid shape, rather than the typical spindle-like appearance (Rensen et al., 2007). In addition, we observed a significant increase in *EDN1* transcript and EDN1 secretion, as well as *MYHCII* expression. Differences in cell morphology during differentiation and further analysis suggests that the *HIF2A* mutation results in different phenotypes in HIF2-SMCs both early on in development and at the end of differentiation. This may be due to HIF2A accumulation causing a more stressful environment for SMCs during differentiation, leading to changes in phenotype. These findings further highlight the use of iPSCs as a powerful tool in disease modeling and translational medical research (Soldner and Jaenisch, 2012) and as a platform to monitor the impact of the *EPAS1 GOF* mutations during SMC development (Dash et al., 2015; Soldner and Jaenisch, 2012).

On the molecular level, it is evident that the *HIF2A* GOF mutations lead to higher expression of the potent vasoconstrictor, *EDN1*, as well as the cytoskeletal motor protein, *MYHCII*, which could further contribute to the intrinsic stiffness via interactions with F-actin. Another notable finding in our study is that HIF2 SMCs secreted higher levels of EDN1 when compared with WT SMCs. However, SMCs (and ECs) generated from two independent sets of hiPSC lines demonstrated different baseline secretions of EDN1 (an average of 2 pg/mL for WT-SMCs in comparison to 15 pg/mL for F-WT-SMCs). This could be due to either patient-to-patient variability or a discrepancy caused by different hiPSC reprogramming methods. Despite the differences in baseline levels, significantly higher amounts of secreted EDN1 were found across the board in HIF2-SMCs when compared with WT-SMCs. Altogether, these results demonstrated that the diseased SMC phenotype potentially contributes to vascular stiffening, independent of endothelial dysfunction.

However, on the extracellular level, we found increased expression of ECM proteins including elastin, fibrillin-1, and fibronectin in these diseased SMCs, while observing lower transcript levels of *COLI* and *COLIII* (Rensen et al., 2007). HIF2-SMCs were found to be much stiffer when measured by AFM. In HIF2-SMCs cultured *in vitro*, stiffness is most likely an effect of the cytoskeletal changes. Individually assessing the SMCs *in vitro* allowed us to demonstrate that the *HIF2A* GOF mutation can induce changes in SMC to the stiffness independent of endothelial dysfunction (Sehgel et al., 2013). We propose that the increase in stiffness could be due to an increase of F-actin polymerization and increased actin-myosin interaction induced by high levels of EDN1 (Xiang et al., 2010). A plausible mechanism may be that high levels of

EDN1 binding to the $ET_A$ receptor leads to increased actin and myosin formation and interactions, thus generating increased cytoskeletal tension.

Although we have investigated the effects of the *HIF2A* mutation in ECs and SMCs respectively, the interaction between ECs and SMCs, as in blood vessels, is critical for maintaining proper function via paracrine signaling between the endothelium and the mural cells. By co-culturing these two cell types, a more comprehensive understanding of the effects of *HIF2A* mutation in vascular stiffening can be elucidated. We created four different co-culture combinations to examine if there was any compensation on the vasodilator-vasoconstrictor levels in the SMCs in the presence of WT-ECs or an even greater imbalance when cultured with HIF2-ECs. Our findings show that when HIF2-SMCs were co-cultured with WT-ECs, a reduction of *EDN1* transcript level occurred. This could be a compensative effect exerted from the WT-ECs that increases vasodilator expression in the co-culture environment. On the other hand, when HIF2-ECs were co-cultured with HIF2-SMCs, we noticed an increase in *EDN1* expression, mimicking the effect of vascular stiffening. When WT-SMCs were cultured with HIF2-ECs, no significant difference was found in the expression level of *EDN1*. When WT-ECs or HIF2-ECs were cultured alone, their respective EDN1 secretion level is comparable to each other and in general is 100-fold higher than the EDN1 secretion level of their SMC-counterpart that are cultured alone. Upon co-culturing with SMCs, the level of EDN1 secretion is significantly lowered in all co-culture combinations. An interesting perspective is that SMCs play a crucial role in determining the EDN1 secretion, as our observations indicate that the SMC source (either WT or HIF2), but not the EC source, dictates secreted EDN1 levels, in that co-culture combinations including HIF2-SMCs always secrete higher concentration of EDN1 when compared with co-culture combinations with WT-SMCs. Altogether, our findings suggest that *HIF2A* mutation affects SMC functionality and interactions. Although considerations must be made in the co-culture model for factors such as absence of growth factors and low serum content in the co-culture medium, we have successfully detected changes in the vasoconstrictor and vasodilator transcript levels, suggesting a new role for SMCs in blood vessels. Thus, our results establish and validate the use of this co-culture model from future studies analyzing interaction between ECs and SMCs in different disease backgrounds.

Both *HIF2A* GOF-mutated patients and *Hif2a* knock-in mice develop vascular complications later in life. As an attempt to isolate the effect of *HIF2A* mutation in regulating SMC stiffness, we assessed HIF2A siRNA knockdown, Bosentan treatment, and $ET_A$/$ET_B$ siRNA knockdown. Although various studies have shown a relationship between HIF1A and EDN1 (Chester and Yacoub, 2014; Pisarcik et al., 2013), determining the functional interactions between HIF2A and EDN1 is crucial for the pathogenesis of vascular stiffening in PH, which was induced by the accumulation of HIF2A (Kapitsinou et al., 2016a). Through *HIF2A* siRNA knockdown studies we found an unequivocal reduction in the gene expression of *EDN1*, demonstrating that *EDN1* activation is dependent upon HIF2A. *HIF2A* siRNA knockdown also reduced the expression of cytoskeletal proteins including acetylated alpha-tubulin and SMA, shown via immunoblots. Although it is known that the HIFs regulate vascular remodeling, through our work, it is evident that HIF2A stabilization is also responsible for the activation of vasoactive substances that contribute to the onset of vascular stiffening. Cell treatment with the EDN1 receptor antagonist Bosentan was performed to test the immediate downstream effects of EDN1. It was apparent that Bosentan treatment significantly reduced the stiffness of HIF2-SMCs, as shown by the reduced overall expression of cytoskeletal proteins associated with stiffness and AFM measurements. The results demonstrated by siRNA and drug treatment clearly show that activation of EDN1 is dependent upon HIF2A induction, which then leads to the most notable characteristics of vascular stiffening in PH such as increased cellular stiffness through increased cytoskeletal tension. Our data pertaining to the stiffening of SMCs in the diseased state is further validated by the increased expression of cytoskeleton proteins and ECM deposition (Thomas et al., 2013; Lee et al., 1998). As many drugs may have non-specific effects, $ET_A$/$ET_B$ siRNA knockdown experiments were performed to mimic the desired effects of Bosentan. As Bosentan is primarily a receptor antagonist of $ET_A$, a 2:1 ratio of $ET_A$:$ET_B$ was chosen. $ET_B$ siRNA was still used, as it has been shown that Bosentan binds to the receptor but with decreased efficiency. Despite following similar trends for *EDN1*, *APLN*, and *MYHCII*, the significant increase in *ELN* expression could be a result of increased $ET_B$ binding in comparison to that found in Bosentan, leading to vasodilation and anti-proliferation (Schneider et al., 2007). ELN is known to be involved in these processes (Faury et al., 1997; Wagenseil and Mecham, 2012). Overall, similar trends were observed with the siRNA treatments, reducing the possibility of our results being caused by non-specific effects of Bosentan and supporting HIF2A GOF mutations increasing SMC stiffness via the EDN1 pathway.

To further assess the impact of the *HIF2A* GOF mutations at the cellular level, we used *HIF2A* GOF mice, which have been shown to develop erythrocytosis, pulmonary hypertension, and increased right ventricular heart thickness. In our studies, we focused on young *Hif2a* mice to examine whether we could detect early onset of vascular complications. Indeed, 8- to 16-week-old mice had early signs of pulmonary hypertension. Isolated SMCs from the mPA of *Hif2a* mice were stiffer than SMCs isolated from mPA of their WT counterparts. *Hif2a* heterozygous mouse SMCs also exhibited more disorganized stress fibers than their WT counterparts. To determine if the effects wrought by *HIF2A* GOF mutations at the cellular level translate to *in vivo* vascular mechanical deficits, we examined vascular segments from Hif2A heterozygous mice. Our studies showed more mPA deformation in the *Hif2a* heterozygous mice when compared with WT mice. Closer examination of the *Hif2a* heterozygous mPA's indicated that there were no tissue-level differences evident from histology but *Hif2a* heterozygous vasculature did contain higher ELN/Col3a1 and Col1a1/Col3a1 ratios overall, suggesting cellular-level differences in ECM product ratios. Together, these findings suggest that SMC stiffening and dysfunction precede any changes to the overall mPA tissue structure in the *HIF2a* GOF mice.

In future studies, we will evaluate how aging further exacerbates pulmonary hypertension and drives aberrant mechanics of the PA via ECM deposition and remodeling, which can contribute to right heart failure. Although our study shows an overall increase in SMCs stiffness, future studies should look into investigating the upstream regulators of SMC stiffness on the intracellular and extracellular levels.

In summary, our study demonstrates a unique perspective that a *HIF2A* GOF mutation alone is sufficient to induce diseased phenotypes of SMCs. An overall increase in SMC stiffness is mainly contributed by increased F-actin stress fibers, SMMHC, and increased acetylated alpha-tubulin in HIF2-SMCs when compared with WT-SMCs. Evidence from our study indicates that increased stiffness is strongly correlated to the increase in EDN1 concentration, which is upregulated when HIF2A is stabilized in SMCs. In *in vivo* studies, Hif2A GOF heterozygous mice show onset of pulmonary hypertension, aberrant SMCs, and vascular mechanics compared with wild-type mice, pointing to the role that SMCs play in vascular homeostasis.

## Limitations of the study

These studies clearly show that HIF2A GOF mutations lead to increased EDN1 secretion and signaling, and that increased EDN1 secretion leads to increased F-actin stress fibers and increased stiffness in SMCs. However, additional studies are needed to determine a singular molecular mechanism for how HIF2A GOF mutations lead to increased EDN1 levels. Our *in vivo* studies indicate Hif2a heterozygous mice have differences in mRNA levels for common ECM components and exhibit pulmonary hypertension. Nonetheless, additional studies must be performed to determine how Hif2a heterozygous mice have higher endogenous ratios of ELN/COL3a1 and Col1a1/Col3a1 but no similar measurable differences on the histological scale. Furthermore, additional studies are needed to stablish causality between different levels of ELN, Col1a1, and Col3a1 and pulmonary hypertension.

## Resource availability

### *Lead contact*

Further information, requests, and inquiries should be directed to and will be fulfilled by the lead contact, Dr. Sharon Gerecht (gerecht@jhu.edu).

### *Materials availability*

All tables and figures are included in the text and supplemental information.

### *Data and code availability*

The published article contains all data generated or analyzed.

## METHODS

All methods can be found in the accompanying transparent methods supplemental file.

## SUPPLEMENTAL INFORMATION

Supplemental information can be found online at https://doi.org/10.1016/j.isci.2021.102246.

## ACKNOWLEDGMENTS

We thank Bin Sheng Wong, Quinton Smith, and Julia Ju for helpful discussions throughout this work; Colin Maguire for helpful discussions about the new hiPSC lines; Koreana Pak for western blot analysis; Anna Coughlan, Quinton Smith, and Dong Ho Shin for help with image analyses; Chris Yankaskas and Michele Vitolo for help with the AFM measurements; Bin-Kuan Chou for assisting with iPSC generation; J.S. for genotyping familial hiPSCs; and Linda Procell for assisting with mouse surgeries, histological imaging, and quantification. This work is supported by a Fellowship from the Johns Hopkins University Applied Physics Laboratory (to E.V.), American Heart Association 20POST35180102 and National Institutes of Health (NIH) training grant 5T32HL007227 (to B.L. Lin), NRSA F32 postdoctoral fellowship F32HL128038 (to X. Y. Chan) from the NIH/National Heart, Lung, and Blood Institute, R01-DK104796 (to F.S. Lee), MSCRFI-2784 from Maryland Stem Cells Research Fund, and 15EIA22530000 from American Heart Association (to S.G.).

## AUTHOR CONTRIBUTIONS

Conceptualization, X.Y.C., E.V., J.E., S.G.; Methodology, X.Y.C., J.E., E.V., L.S., S.G.; Investigation, X.Y.C., J.E., E.V., L.F., R.B., R.G., S.F.B.O., J.C., M.E., Formal Analysis, X.Y.C., J.E., E.V., L.F., R.B., R.G.,B.L.L., S.F.B.O., J.C., M.E., J.S.; Resources, L.C., F.S.L., J.T.P., S.G.; Writing—Original Draft, X.Y.C., J.E., E.V., S.G.; Writing—Review & Editing, X.Y.C., J.E., E.V., M.E., S.G.; L.S., J.T.P., F.S.L., and S.G.

## DECLARATION OF INTERESTS

The authors declare no competing interests.

Received: August 27, 2020
Revised: October 26, 2020
Accepted: February 25, 2021
Published: April 23, 2021

## REFERENCES

Berkowitz, D.E., White, R., Li, D., Minhas, K.M., Cernetich, A., Kim, S., Burke, S., Shoukas, A.A., Nyhan, D., Champion, H.C., and Hare, J.M. (2003). Arginase reciprocally regulates nitric oxide synthase activity and contributes to endothelial dysfunction in aging blood vessels. Circulation *108*, 2000–2006.

Bohm, F., and Pernow, J. (2007). The importance of endothelin-1 for vascular dysfunction in cardiovascular disease. Cardiovasc. Res. *76*, 8–18.

Cacoub, P., Dorent, R., Nataf, P., Carayon, A., Riquet, M., Noe, E., Piette, J.C., Godeau, P., and Gandjbakhch, I. (1997). Endothelin-1 in the lungs of patients with pulmonary hypertension. Cardiovasc. Res. *33*, 196–200.

Chan, X.Y., Black, R., Dickerman, K., Federico, J., Levesque, M., Mumm, J., and Gerecht, S. (2015). Three-dimensional vascular network assembly from diabetic patient-derived induced pluripotent stem cells. Arterioscler. Thromb. Vasc. Biol. *35*, 2677–2685.

Chester, A.H., and Yacoub, M.H. (2014). The role of endothelin-1 in pulmonary arterial hypertension. Glob. Cardiol. Sci. Pract. *2014*, 62–78.

Dai, Z.Y., Li, M., Wharton, J., Zhu, M.M., and Zhao, Y.Y. (2016). Prolyl-4 hydroxylase 2 (PHD2) deficiency in endothelial cells and hematopoietic cells induces obliterative vascular remodeling and severe pulmonary arterial hypertension in mice and humans through hypoxia-inducible factor-2 alpha. Circulation *133*, 2447.

Dash, B.C., Jiang, Z.X., Suh, C., and Qyang, Y.B. (2015). Induced pluripotent stem cell-derived vascular smooth muscle cells: methods and application. Biochem. J. *465*, 185–194.

Ergul, A., Jupin, D., Johnson, M.H., and Prisant, L.M. (2006). Elevated endothelin-1 levels are associated with decreased arterial elasticity in hypertensive patients. J. Clin. Hypertens. (Greenwich) *8*, 549–554.

Faury, G., Chabaud, A., Ristori, M.T., Robert, L., and Verdetti, J. (1997). Effect of age on the vasodilatory action of elastin peptides. Mech. Ageing Dev. *95*, 31–42.

Furchgott, R.F., and Vanhoutte, P.M. (1989). Endothelium-derived relaxing and contracting factors. FASEB J. *3*, 2007–2018.

Furlow, P.W., Percy, M.J., Sutherland, S., Bierl, C., Mcmullin, M.F., Master, S.R., Lappin, T.R., and Lee, F.S. (2009). Erythrocytosis-associated HIF-2alpha mutations demonstrate a critical role for residues C-terminal to the hydroxylacceptor proline. J. Biol. Chem. *284*, 9050–9058.

Gordeuk, V.R., Key, N.S., and Prchal, J.T. (2019). Re-evaluation of hematocrit as a determinant of thrombotic risk in erythrocytosis. Haematologica *104*, 653–658 in press.

Iglarz, M., and Clozel, M. (2007). Mechanisms of ET-1-induced endothelial dysfunction. J. Cardiovasc. Pharmacol. *50*, 621–628.

Kaelin, W.G., Jr., and Ratcliffe, P.J. (2008). Oxygen sensing by metazoans: the central role of the HIF hydroxylase pathway. Mol. Cell *30*, 393–402.

Kapitsinou, P.P., Rajendran, G., Astleford, L., Michael, M., Schonfeld, M.P., Fields, T., Shay, S., French, J.L., West, J., and Haase, V.H. (2016a). The endothelial prolyl-4-hydroxylase domain 2/hypoxia-inducible factor 2 axis regulates pulmonary artery pressure in mice. Mol. Cell. Biol. *36*, 1584–1594.

Kapitsinou, P.P., Rajendran, G., Astleford, L., Schonfeld, M.P., Michael, M., Shay, S., French, J.L., West, J., Haase, V.H., and Fields, T. (2016b). The endothelial Phd2/hif-2 Axis regulates pulmonary artery pressure in mice. J. Invest. Med. *64*, 961–962.

Kim, F.Y., Barnes, E.A., Ying, L., Chen, C., Lee, L., Alvira, C.M., and Cornfield, D.N. (2015). Pulmonary artery smooth muscle cell endothelin-1 expression modulates the pulmonary vascular response to chronic hypoxia. Am. J. Physiol. Lung Cell. Mol. Physiol. *308*, L368–L377.

Kusuma, S., Facklam, A., and Gerecht, S. (2015). Characterizing human pluripotent-stem-cell-derived vascular cells for tissue engineering applications. Stem Cells Dev. *24*, 451–458.

Kusuma, S., Shen, Y.I., Hanjaya-Putra, D., Mali, P., Cheng, L., and Gerecht, S. (2013). Self-organized vascular networks from human pluripotent stem cells in a synthetic matrix. Proc. Natl. Acad. Sci. U S A. *110*, 12601–12606.

Lee, F.S., and Percy, M.J. (2011). The HIF pathway and erythrocytosis. Annu. Rev. Pathol. *6*, 165–192.

Lee, K.M., Tsai, K.Y., Wang, N., and Ingber, D.E. (1998). Extracellular matrix and pulmonary hypertension: control of vascular smooth muscle cell contractility. Am. J. Physiol. *274*, H76–H82.

Lian, X.J., Bao, X.P., Al-Ahmad, A., Liu, J.L., Wu, Y., Dong, W.T., Dunn, K.K., Shusta, E.V., and Palecek, S.P. (2014). Efficient differentiation of human pluripotent stem cells to endothelial progenitors via small-molecule activation of WNT signaling. Stem Cell Rep. *3*, 804–816.

Majmundar, A.J., Wong, W.J., and Simon, M.C. (2010). Hypoxia-inducible factors and the response to hypoxic stress. Mol. Cell *40*, 294–309.

Mas, M. (2009). A close look at the endothelium: its role in the regulation of vasomotor tone. Eur. Urol. Supplements *8*, 48–57.

Pisarcik, S., Maylor, J., Lu, W., Yun, X., Undem, C., Sylvester, J.T., Semenza, G.L., and Shimoda, L.A. (2013). Activation of hypoxia-inducible factor-1 in pulmonary arterial smooth muscle cells by endothelin-1. Am. J. Physiol. Lung Cell. Mol. Physiol. *304*, L549.

Rensen, S.S., Doevendans, P.A., and Van Eys, G.J. (2007). Regulation and characteristics of vascular smooth muscle cell phenotypic diversity. Neth. Heart J. *15*, 100–108.

Sandoo, A., Van Zanten, J.J., Metsios, G.S., Carroll, D., and Kitas, G.D. (2010). The endothelium and its role in regulating vascular tone. Open Cardiovasc. Med. J. *4*, 302–312.

Schneider, M.P., Boesen, E.I., and Pollock, D.M. (2007). Contrasting actions of endothelin ET(A) and ET(B) receptors in cardiovascular disease. Annu. Rev. Pharmacol. Toxicol. *47*, 731–759.

Sehgel, N.L., Zhu, Y., Sun, Z., Trzeciakowski, J.P., Hong, Z., Hunter, W.C., Vatner, D.E., Meininger, G.A., and Vatner, S.F. (2013). Increased vascular smooth muscle cell stiffness: a novel mechanism for aortic stiffness in hypertension. Am. J. Physiol. Heart Circ. Physiol. *305*, H1281–H1287.

Semenza, G.L. (2001). Hypoxia-inducible factor 1: oxygen homeostasis and disease pathophysiology. Trends Mol. Med. *7*, 345–350.

Sergueeva, A.I., Miasnikova, G.Y., Polyakova, L.A., Nouraie, M., Prchal, J.T., and Gordeuk, V.R. (2015). Complications in children and adolescents with Chuvash polycythemia. Blood *125*, 414–415.

Smith, Q., Chan, X.Y., Carmo, A.M., Trempel, M., Saunders, M., and Gerecht, S. (2017). Compliant substratum guides endothelial commitment from human pluripotent stem cells. Sci. Adv. *3*, e1602883.

Soldner, F., and Jaenisch, R. (2012). Medicine. iPSC disease modeling. Science *338*, 1155–1156.

Tan, Q., Kerestes, H., Percy, M.J., Pietrofesa, R., Chen, L., Khurana, T.S., Christofidou-Solomidou, M., Lappin, T.R., and Lee, F.S. (2013). Erythrocytosis and pulmonary hypertension in a mouse model of human HIF2A gain of function mutation. J. Biol. Chem. *288*, 17134–17144.

Thomas, G., Burnham, N.A., Camesano, T.A., and Wen, Q. (2013). Measuring the mechanical properties of living cells using atomic force microscopy. J. Vis. Exp. *27*, 50497.

Tuder, R.M., Marecki, J.C., Richter, A., Fijalkowska, I., and Flores, S. (2007). Pathology of pulmonary hypertension. Clin. Chest Med. *28*, 23–42, vii.

Vo, E., Hanjaya-Putra, D., Zha, Y., Kusuma, S., and Gerecht, S. (2010). Smooth-muscle-like cells derived from human embryonic stem cells support and augment cord-like structures in vitro. Stem Cell Rev. Rep. *6*, 237–247.

Wagenseil, J.E., and Mecham, R.P. (2012). Elastin in large artery stiffness and hypertension. J. Cardiovasc. Transl. Res. *5*, 264–273.

Wanjare, M., Kuo, F., and Gerecht, S. (2013). Derivation and maturation of synthetic and contractile vascular smooth muscle cells from human pluripotent stem cells. Cardiovasc. Res. *97*, 321–330.

Wanjare, M., Kusuma, S., and Gerecht, S. (2014). Defining differences among perivascular cells derived from human pluripotent stem cells. Stem Cell Rep. *2*, 561–575.

Wenger, R.H., and Hoogewijs, D. (2010). Regulated oxygen sensing by protein hydroxylation in renal erythropoietin-producing cells. Am. J. Physiol. Ren. Physiol. *298*, F1287–F1296.

Xiang, Y., Li, B., Li, G.G., Wang, R.L., Chen, Z.Q., Xu, L.J., Chen, L., Shi, H., and Zhang, H. (2010). Effects of endothelin-1 on the cytoskeleton protein F-actin of human trabecular meshwork cells in vitro. Int. J. Ophthalmol. *3*, 61–63.

**iScience, Volume *24***

## Supplemental information

# *HIF2A* gain-of-function mutation modulates the stiffness of smooth muscle cells and compromises vascular mechanics

**Xin Yi Chan, Eugenia Volkova, Joon Eoh, Rebecca Black, Lilly Fang, Rayyan Gorashi, Jihyun Song, Jing Wang, Morgan B. Elliott, Sebastian F. Barreto-Ortiz, James Chen, Brian L. Lin, Lakshmi Santhanam, Linzhao Cheng, Frank S. Lee, Josef T. Prchal, and Sharon Gerecht**

## Supplemental Information

## Supplemental Figures

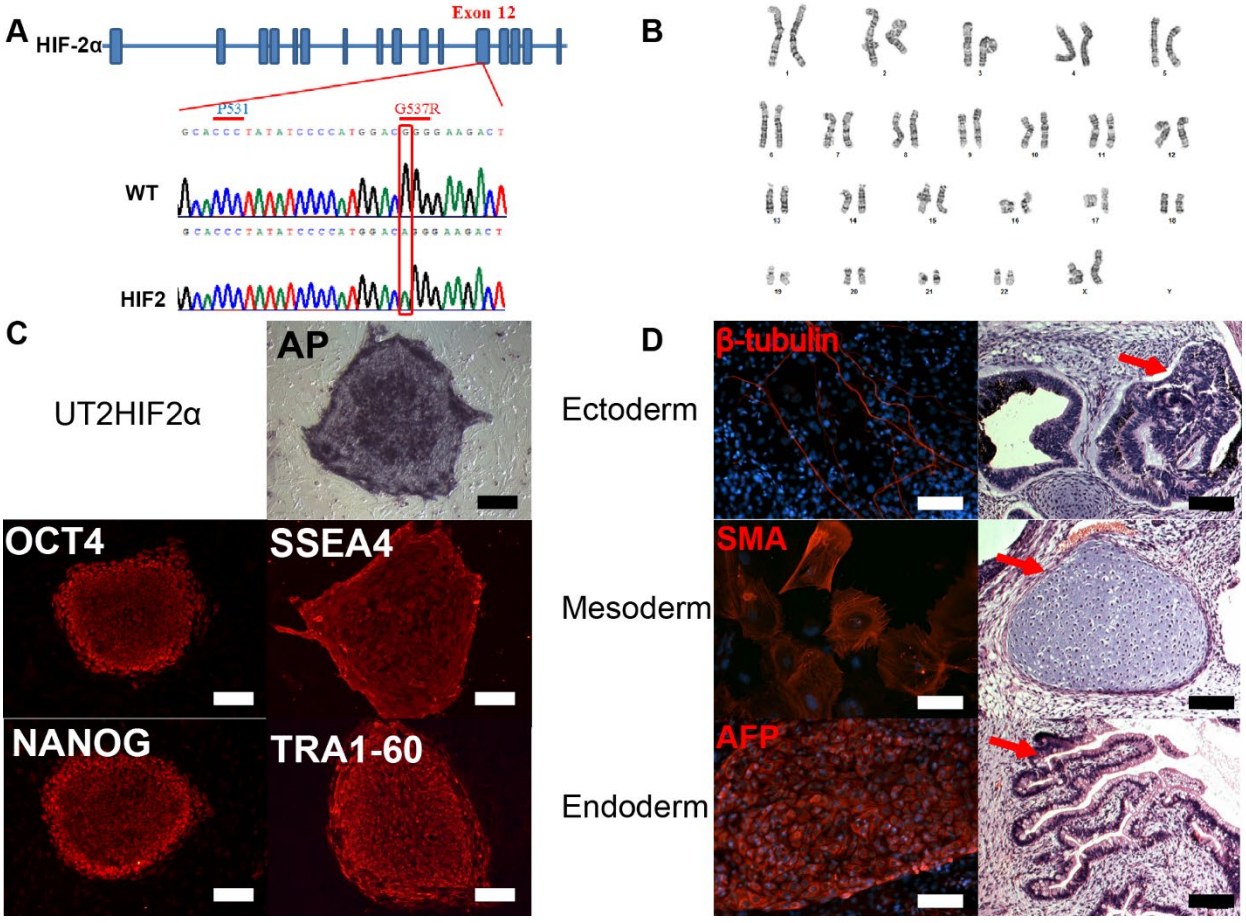


**Figure S1. Generation of UT2HIF2α iPSC from patient with erythrocytosis, Related to Figure 1**

(**A**) UT2HIF2α iPSC has a heterozygous single mutation of G537R (G-->A) on exon 12 of *HIF2A* gene. (**B**) Normal karyotype of UT2HIF2α iPSC. (**C**) Detection of AP activity and Immunofluorescence staining of pluripotency markers: OCT4, SSEA4, NANOG and TRA1-60. (**D**) Spontaneous differentiation of UT2HIF2α cells into different germ layer. Hematoxylin and Eosin staining of teratoma sections shows neuronal rosette, cartilage and gut-like epithelium. Scale bars are 50μm.

**Supplementary Figure 2**

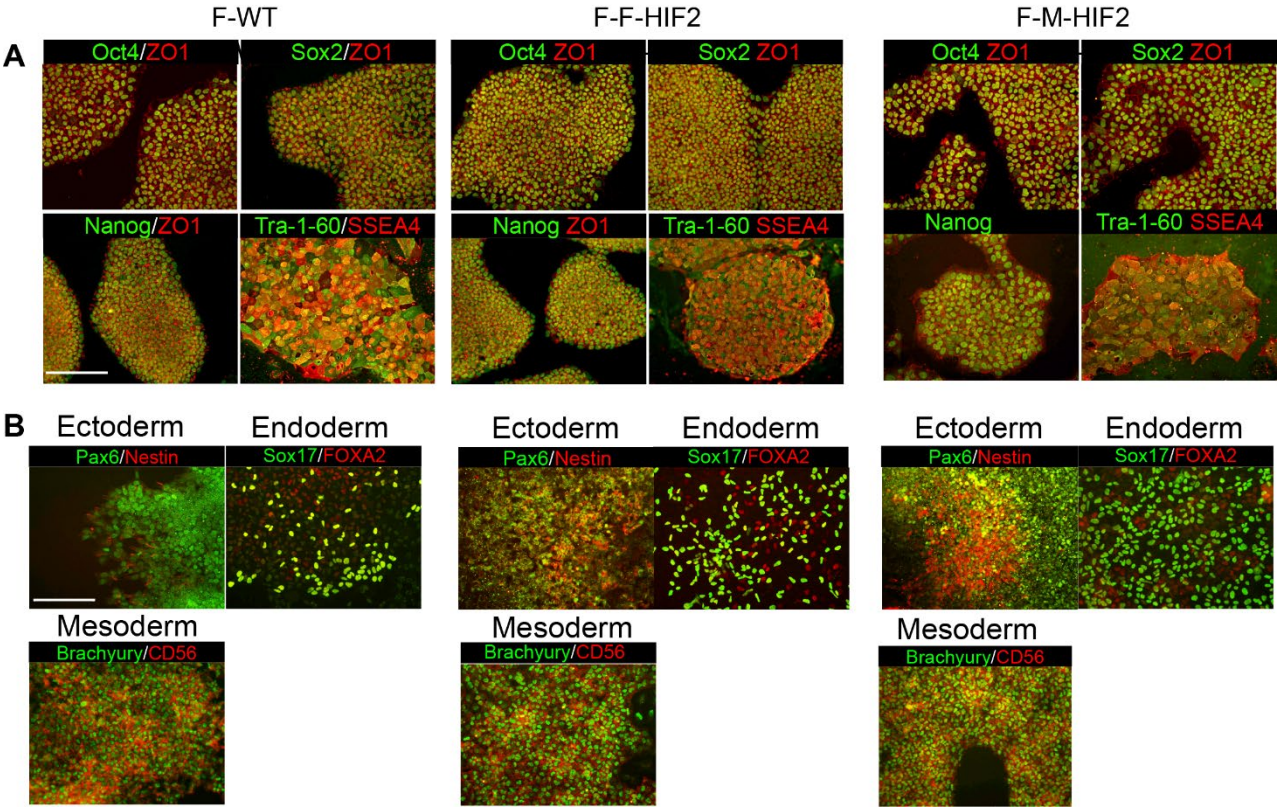


**Figure S2. Generation of F-HIF2- and F-WT hiPSC lines, Related to Figure 1** (**A**) Pluripotent assay: IF of pluripotent markers: Oct4, Sox2, Nanog, Tra-1-60 and SSEA4. (**B**) Tri-lineage differentiation assay: IF of three germ layers markers. All scale bars at 200μm.

**Supplementary Figure 3**

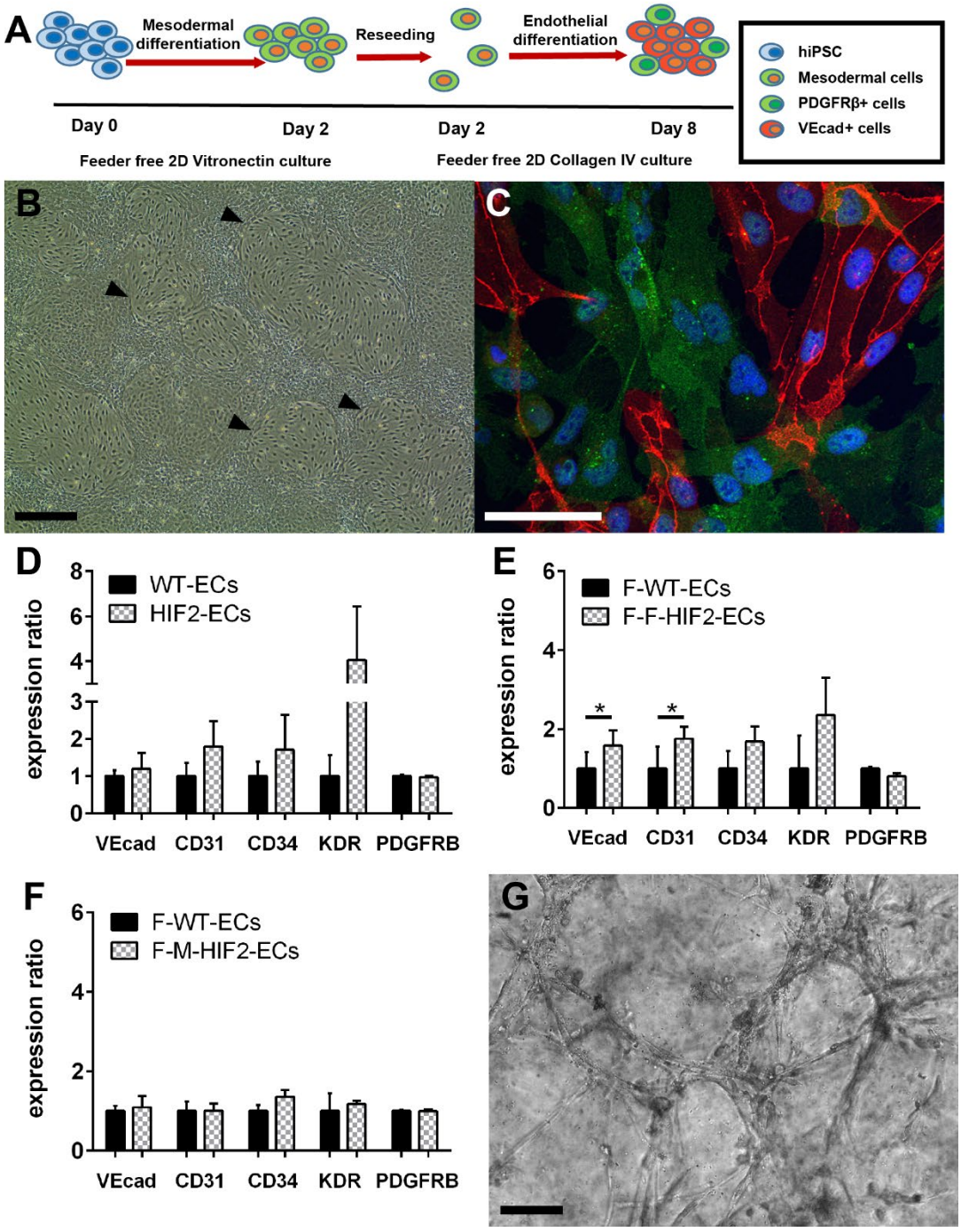


**Figure S3. Early vascular cells (EVC) differentiation of HIF2-hiPSCs, Related to Figure 3** (**A**) EVC differentiation scheme. (**B**) LM image of HIF2-EVCs in the end of the differentiation. Scale bar is 100μm. (**C**) IF image of day 8 HIF2-EVCs. VEcad (red), PDGFRB (green), DAPI (blue). Scale bar is 20μm. Flow cytometry of vascular marker expression of (**D**) WT-EVCs vs. HIF2-EVCs and (**E**) F-WT-EVCs vs F-F-HIF2-EVCs and (**F**) F-WT-EVCs vs F-M-HIF2-EVCs on day 6 of EVC differentiation. (**F**) HIF2-EVCs self-assembled to form network when embedded in collagen I

hydrogel. Data is represented as mean +/- standard deviation. Significance level is set at *p<0.05 for a two-tailed t-test. Scale bar is 100μm.

**Supplementary Figure 4**

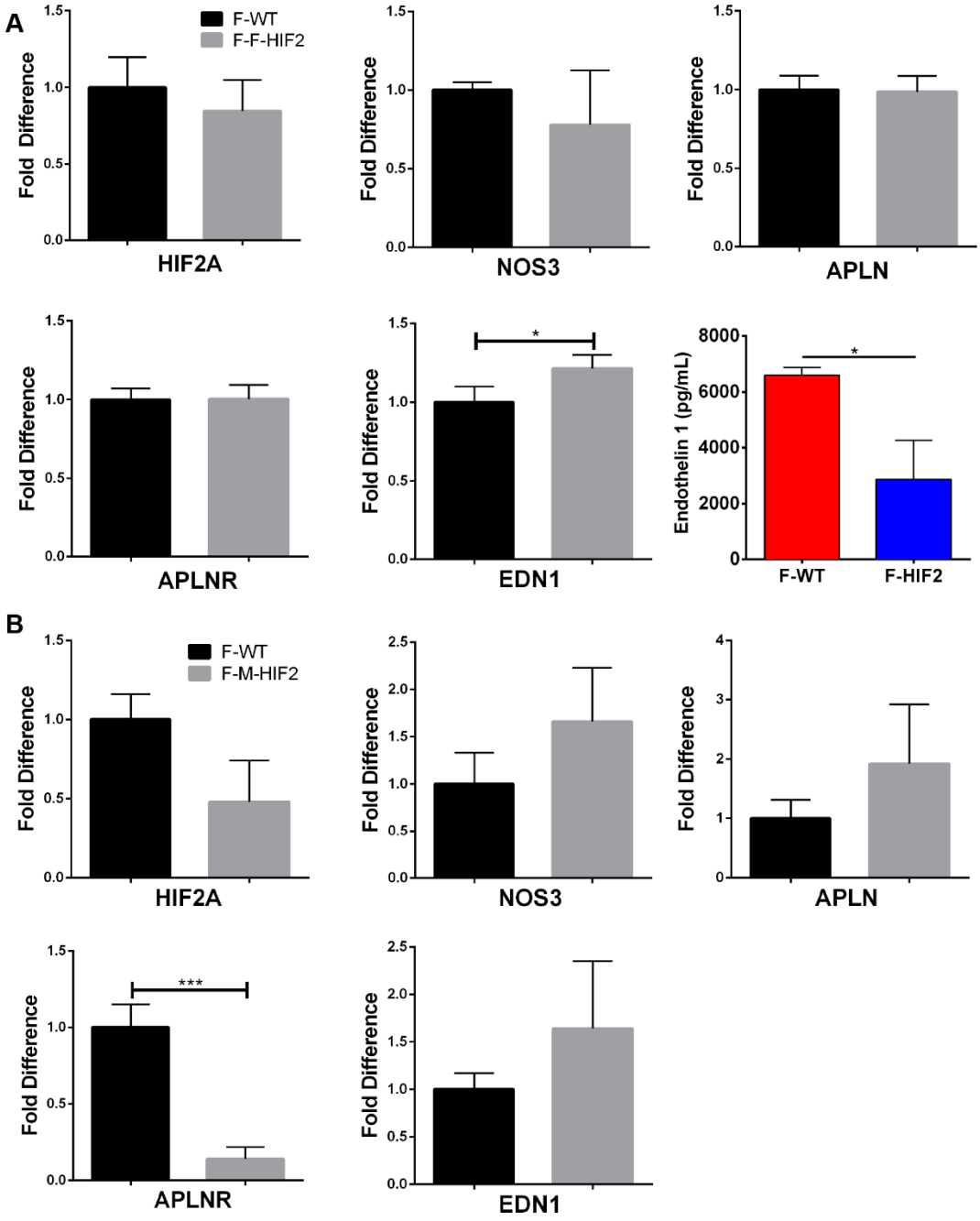


**Figure S4. Expression of vasodilators and vasoconstrictors in F HIF2 ECs, Related to Figure 3.** (**A**) qPCR of F-F-HIF2-ECs and quantification of EDN1 level in F-WT-ECs and F-F-

HIF2-ECs using ELISA (n=3). The data are presented as fold-change difference in reference to F-WT-ECs. Expression levels were normalized to internal control *GAPDH* expression level (n=3). Significance level is set at *p<0.05. (**B**) qPCR of F-M-HIF2-ECs. The data are presented as fold-change difference in reference to F-WT-ECs. Expression levels were normalized to internal control *GAPDH* expression level (n=3). All data is represented as mean +/- standard deviation. Significance level is set at *p<0.05 for a two-tailed t-test.

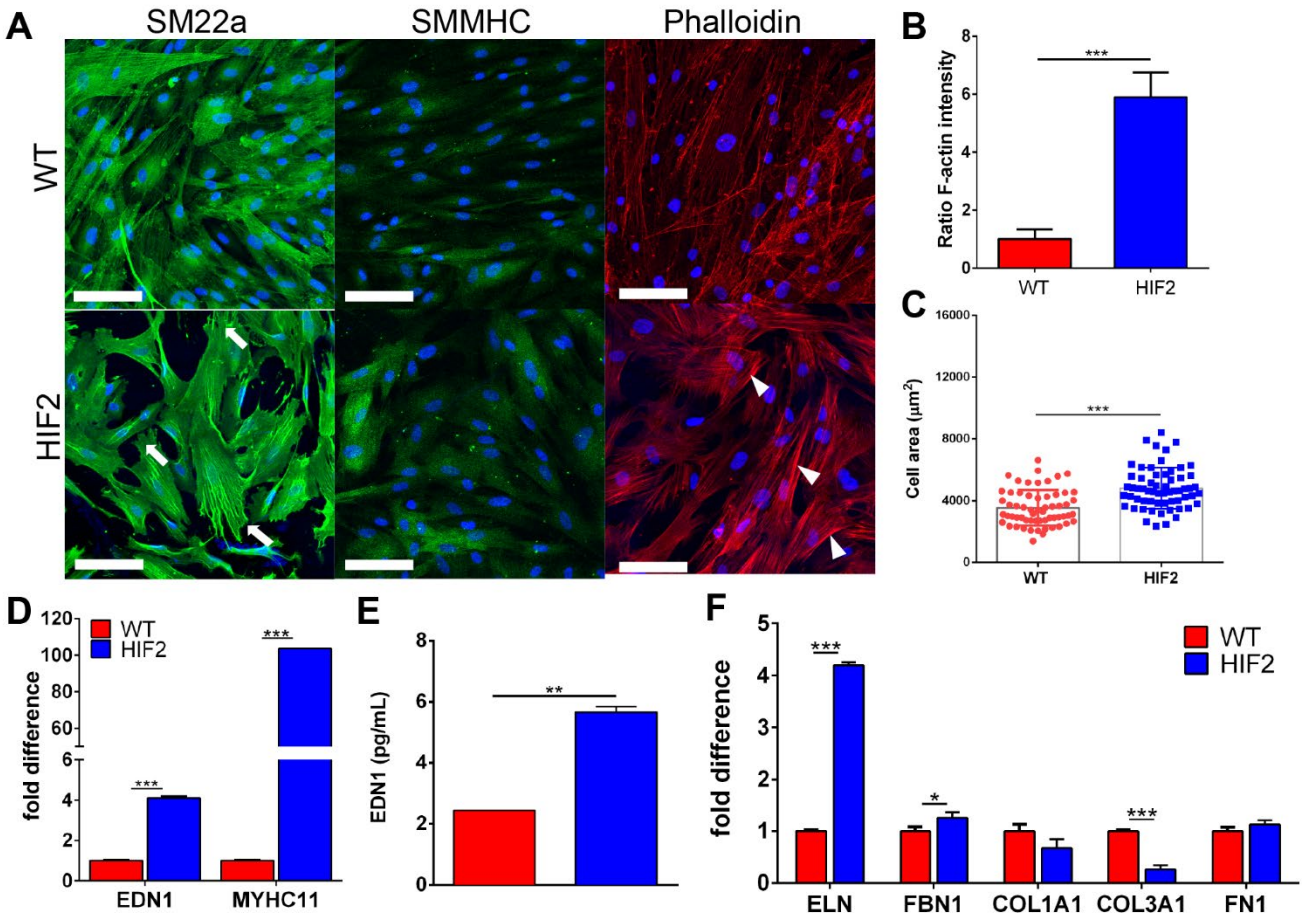


**Figure S5. HIF2-mSMLCs have abnormal phenotype and changes in ECM deposition, Related to Figure 4** (**A**) IF images of SM22a, SMMHC and phalloidin staining. White arrows: jagged borders; white arrowheads: dense actin fibers. (**B**) Quantification of F-actin and (**C**) cell area (n=3). (**D**) qRT-PCR of *EDN1* and *MYHC11*, (**E**) EDN1 secretion in WT and HIF2-mSMLCs (n=5), and (**F**) ECM gene expression. Data are presented as the fold-change difference in reference to WT-mSMLCs. Expression levels were normalized to internal control *GAPDH* expression level (n=3). All data is represented as mean +/- standard deviation. Data in C is additionally represented as individual cell measurements. Significance level is set at ***p<0.001, **p<0.01 and *p<0.05 for a two-tailed t-test. Scale bars are 100μm.

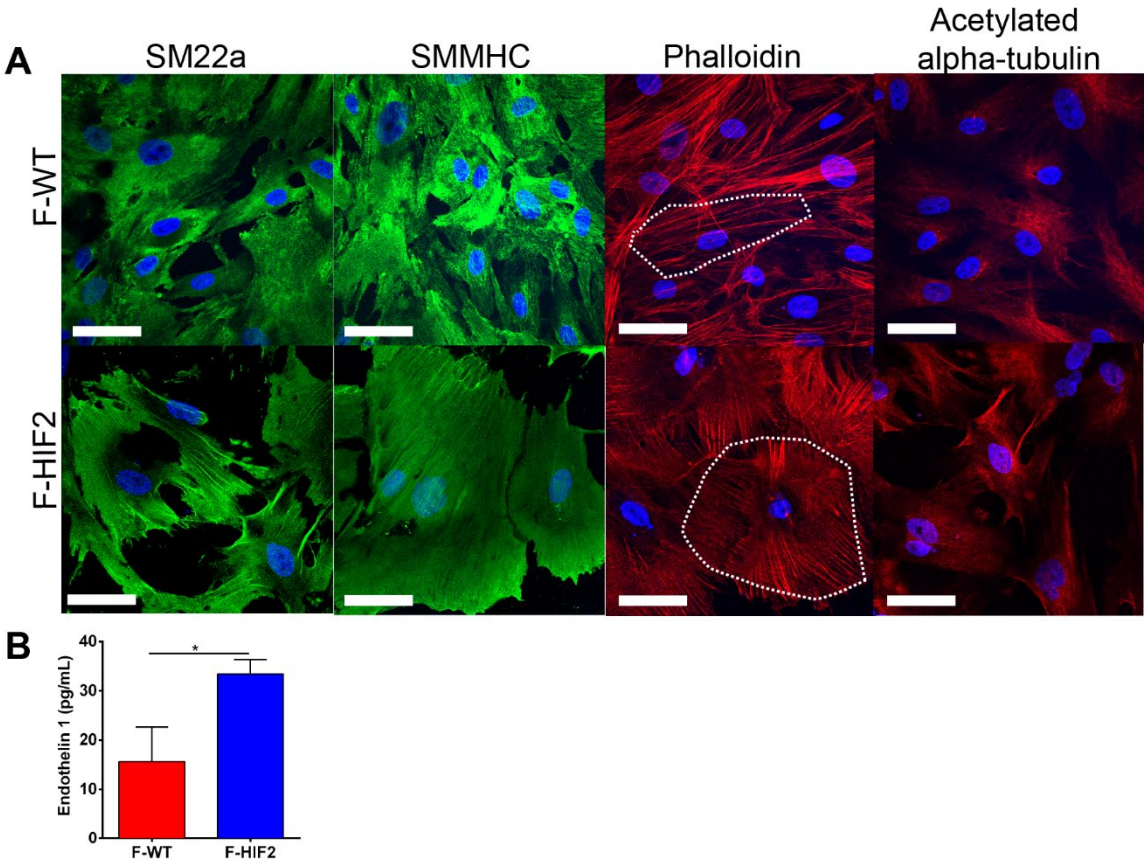


**Figure S6. F-HIF2-SMCs have abnormal phenotypes when compared to F-WT-SMCs, Related to Figure 4** (A) IF images of SM22a, SMMHC, phalloidin and acetylated alpha-tubulin staining. White dotted lines: examples of isotropic fiber arrangement in F-WT-SMCs and anisotropic fiber arrangement in F-HIF2-SMCs. Scale bars are 50μm. (B) Quantification of EDN1 level in F-WT-SMCs and F-HIF2-SMCs using ELISA (n=3). All data is represented as mean +/- standard deviation. Significance level is set at *p<0.05 for a two-tailed t-test.

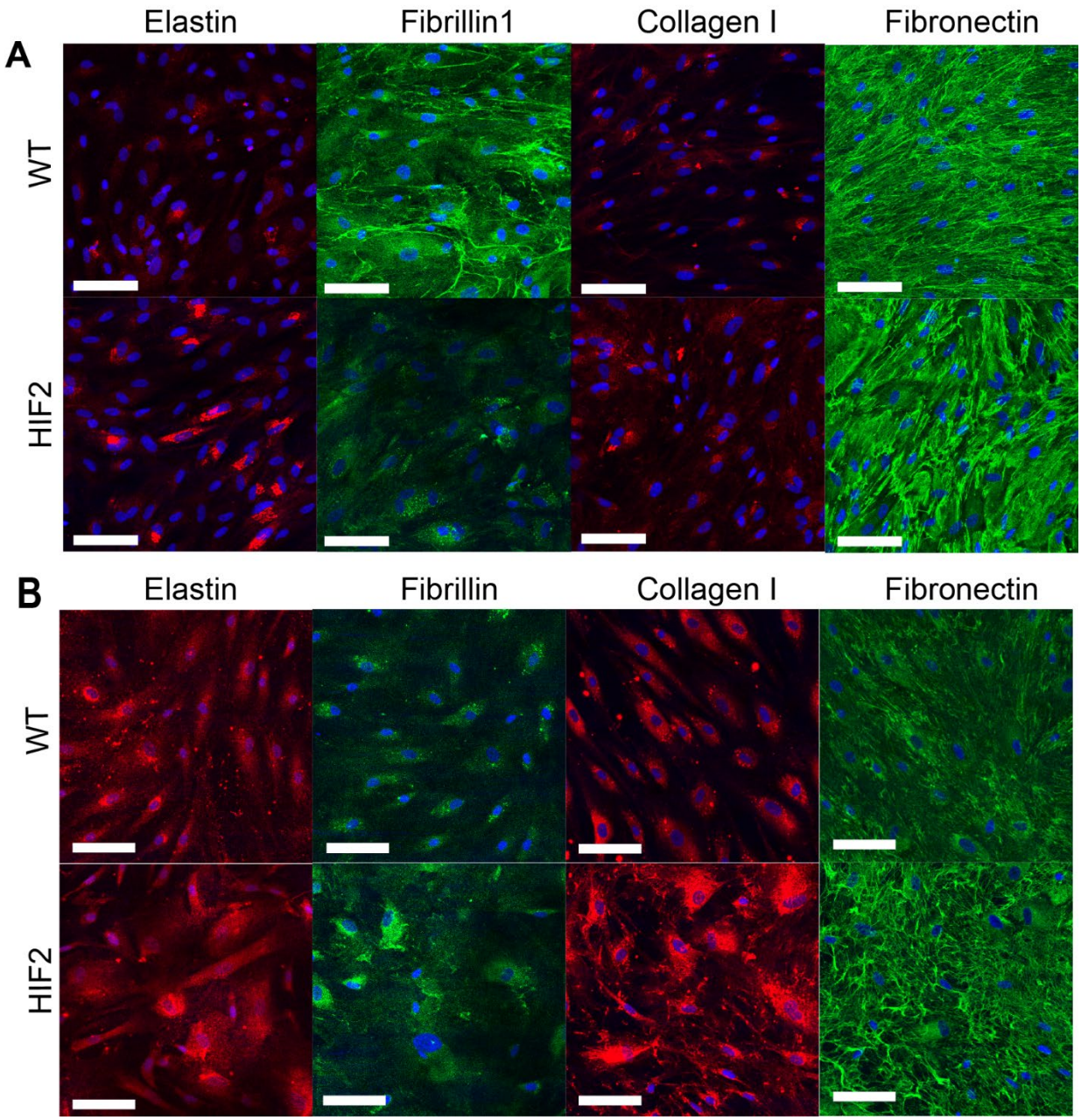


**Figure S7. HIF2-mSMLCs and HIF2-SMCs have different ECM deposition in comparison to WT-mSMLCs and WT-SMCs, Related to Figure 4** (**A**) Representative IF images of ECM deposition in HIF2-mSMLCs in comparison to WT control (n=4). (**B**) Representative IF images of ECM deposition in HIF2-SMCs in comparison to WT control (n=4). Scale bars are 100μm.

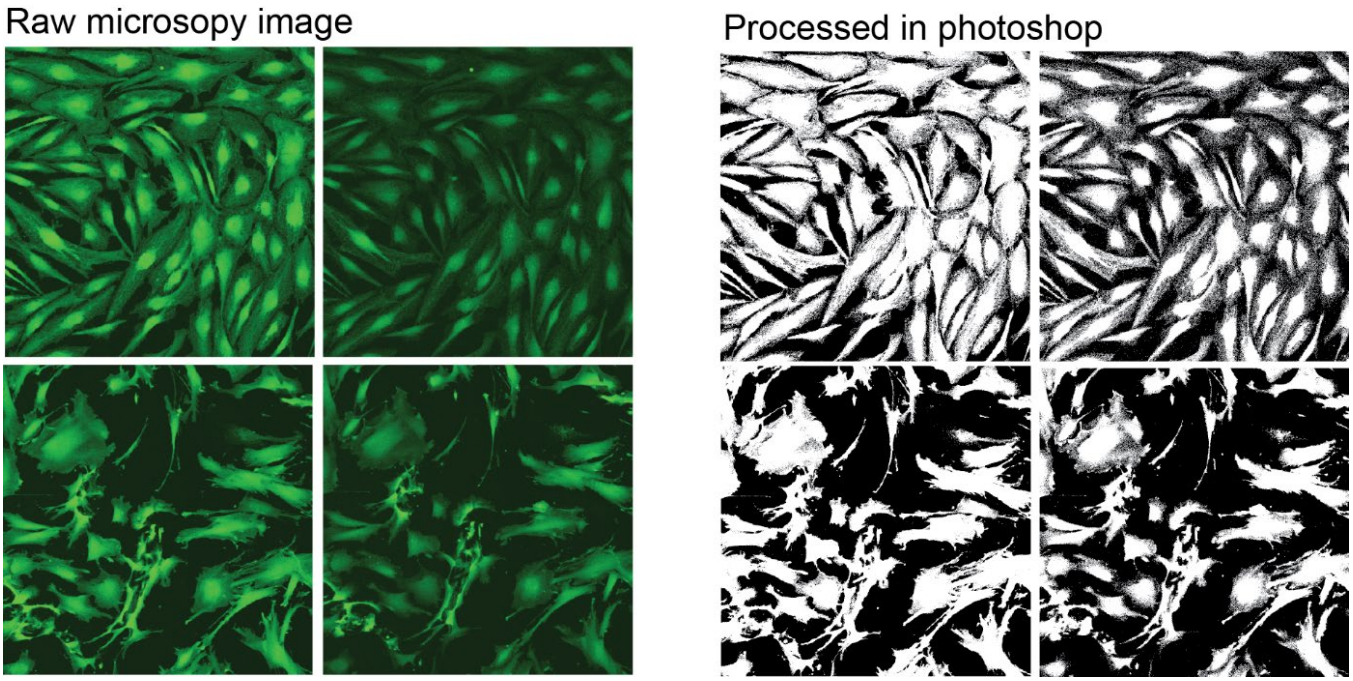


**Figure S8. Carbochol treatment to measure contractility of WT and HIF-SMCs, Related to Figure 4** (**A**) Calcein-AM staining to visualize the cytoplasm. The first and last images of the time-lapse were taken. (**B**) Exported images in Adobe Photoshop CS6 where the green channel of the images were isolated, a threshold for signal detection was established and the area was calculated.

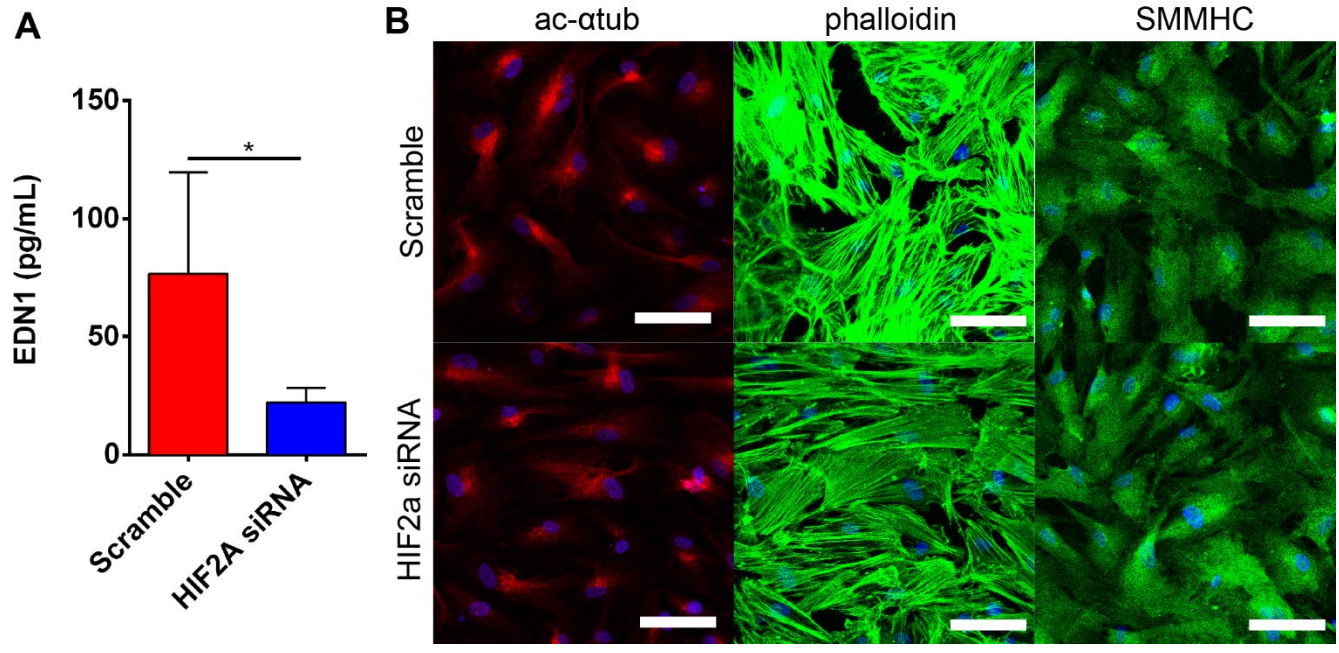


**Figure S9. HIF2A knockdown in HIF2-SMCs, Related to Figure 5 (A) Level of secreted EDN1 protein in HIF2-SMCs treated with scramble control and *HIF2A* siRNA (n=5). Significance level is set at *p<0.05. (B) Representative IF images of cytoskeletal protein expression of**

**control and HIF2α siRNA-treated HIF2-SMCs. Scale bars are 100μm. All data is represented as mean +/- standard deviation. Significance level is set at *p<0.05 for a two-tailed t-test.**

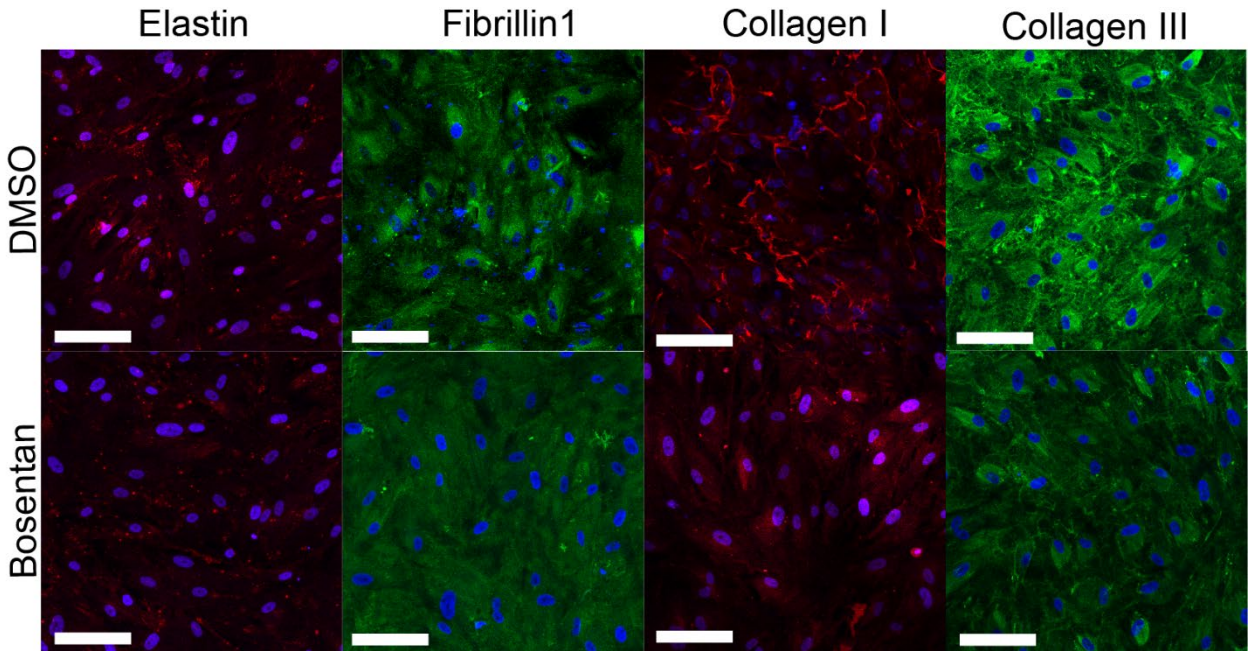


**Figure S10. ECM deposition of HIF2-SMCs control and Bosentan treatment, Related to Figure 5 Representative IF images of ECM deposition in HIF2-SMCs treated with Bosentan in comparison to DMSO control. Scale bars are 100μm.**

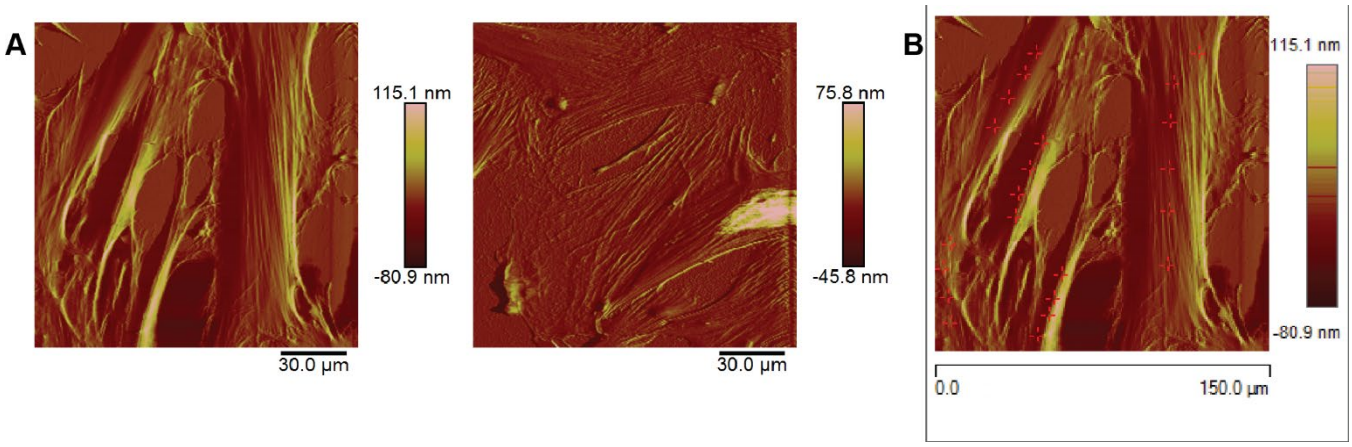


**Figure S11. AFM analysis of DMSO control and Bosentan-treated HIF2-SMCs, Related to Figure 5** (**A**) Representative topography images of DMSO control (left) and Bosentan-treated (right) HIF2-SMCs generated from BioScope Catalyst. (**B**) Representative force measurement points (4-6 points per cell) chosen for each cell.

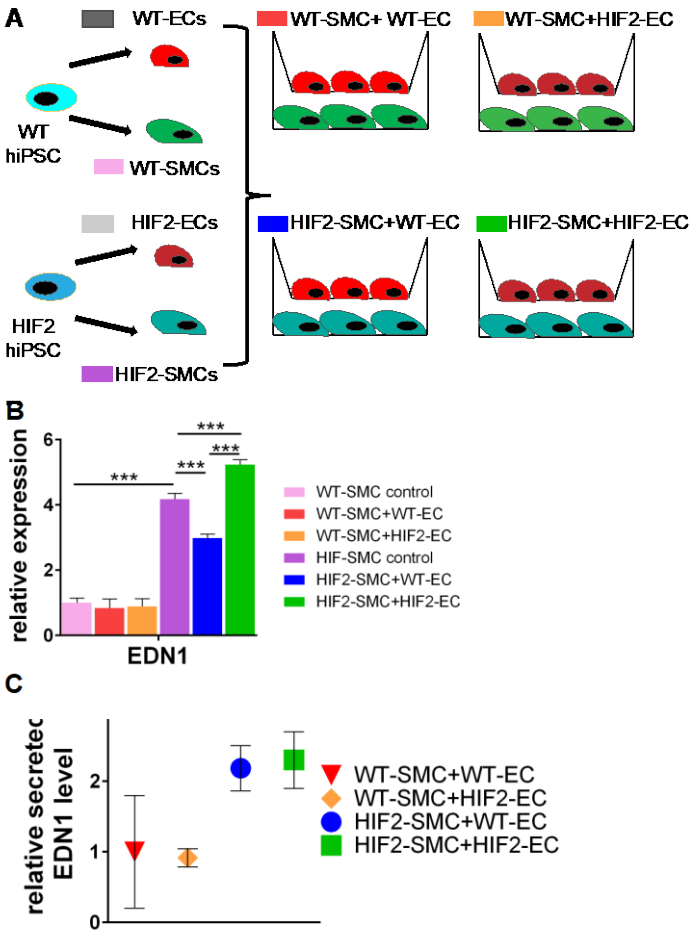


**Figure S12. HIF2 co-culture models of ECs and SMCs, Related to Figure 5** (**A**) Diagram of different combinations of WT or HIF-ECs and WT or HIF-SMCs. (**B**) qRT-PCR data of EDN1 in different combinations of SMC co-cultured with ECs. (n=2). (**C**) Relative EDN1 secretion level normalized to WT-SMC+WT-EC co culture (n=2). All data is represented as mean +/- standard deviation. Significance level is set at ***p<0.001 for a two-tailed t-test.

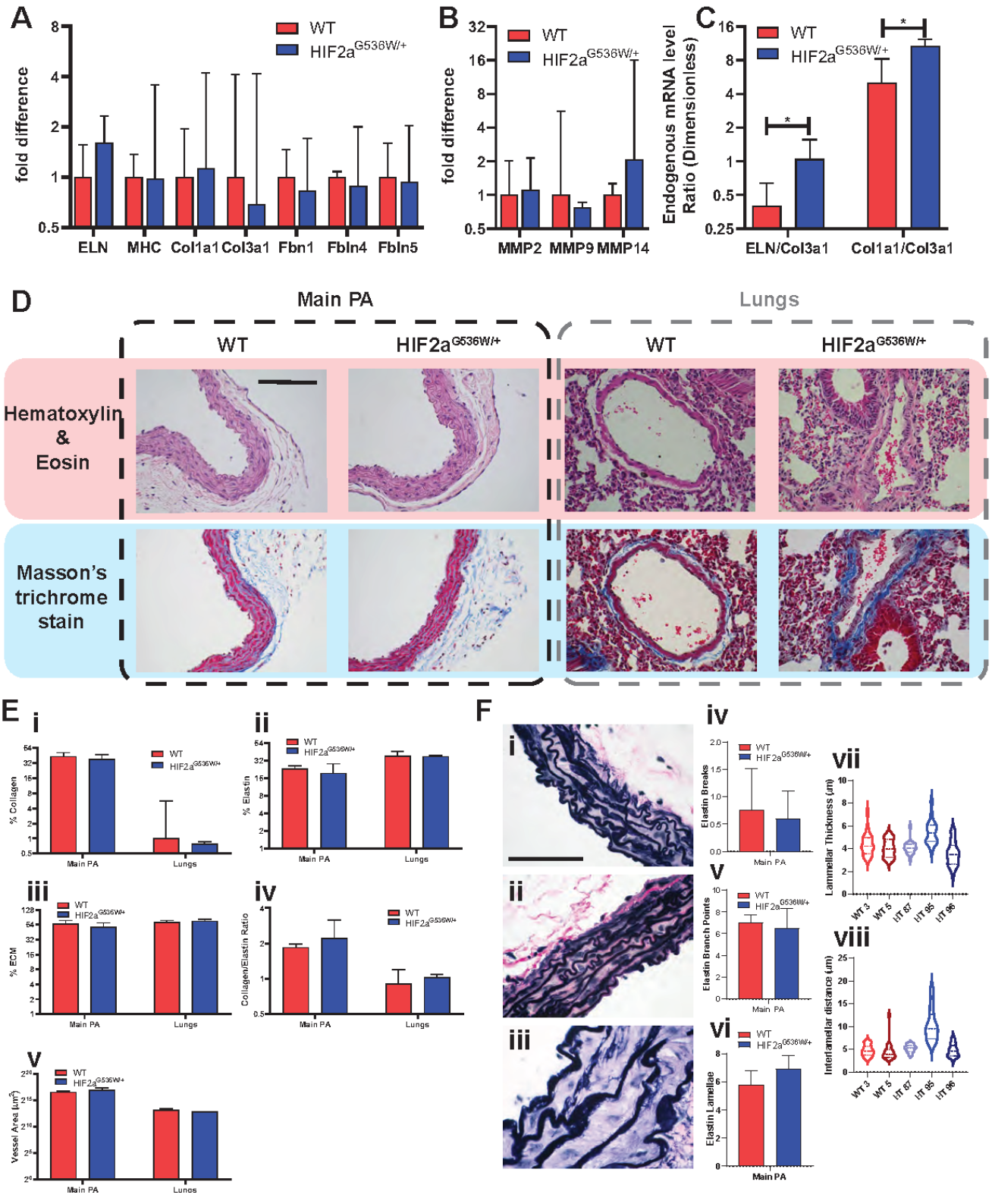


**Figure S13. Potential upstream causes for HIF2A GOF main pulmonary artery deformability, Related to Figure 6** (A) qRT-PCR of relative expression of *ELN, MHC, Col1a1,*

*Col3a1, Fbn1, Fbln4,* and *Fbln5* transcripts in WT and *HIF2a*$^{5336W/+}$ mice (N=3-5). (B) qRT-PCR of relative expression of *MMP2, MMP9,* and *MMP14* transcripts in WT and *HIF2a*$^{5336W/+}$ mouse lungs (N=2). (C) Endogenous mRNA level Ratios for *ELN/COL3a1* and *Col1a1/Col3a1* in WT and *HIF2a*$^{5336W/+}$ mouse lungs (N=4-5). (D) Representative 40x histology images of Hematoxylin & Eosin, Masson's Trichrome, and Verhoeff- Van Gieson stained WT and *HIF2a*$^{5336W/+}$ mouse main pulmonary arteries and lung vasculature. Scale bar is 200 μm. (E) Quantification of histological images of % Collagen (i), % Elastin (ii), % ECM (iii) and Collagen/Elastin ratio (iv) for the medial vessel layer and medial layer cross-sectional vessel area (v) (N=2-3). (F) Representative 100x histology images of Verhoeff-Van Gieson stained WT (i) and *HIF2a*$^{5336W/+}$(ii,iii) mouse main pulmonary arteries. Subsequent quantification of number of elastin breaks (iv), branch points (v), and lamellae (vi) per image (N=2-3). Scale bar is 50 μm. Quantification of lamellar thickness (vii) and interlamellar distance (viii) for individual animals (n=20 images/animal). All data is represented as mean +/- standard deviation. Significance level is set at ***p<0.001, **p<0.01 and *p<0.05 for a two-tailed t-test.

**Transparent Methods section**

**hiPSC derivation and expansion**

With an IRB approved informed consent, mononuclear cells (MNCs) from the peripheral blood of a female patient (labeled as an anonymous donor; UT002) were obtained after phlebotomy treatment at the University of Utah Hospital. It was determined that the patient had an *EPAS1* G537R heterozygous germline mutation, and we obtained consent for using the otherwise discarded blood cells for research. The Cheng lab obtained the MNCs of this anonymous donor (UT002) in 2010 and conducted hiPSC derivation at the Johns Hopkins Medical School. The CD34+ MNCs were cultured and reprogrammed to hiPSCs by transient plasmid expression according to the previously published protocol. (Chou et al., 2011) A fully characterized and validated clone, named HIFA-hiPSC, was used in functional studies described below. A wild-type control hiPSC line, BC1, which was also derived from CD34+ MNCs of a normal donor by the iPSC derivation method, as described previously, was used as an experimental control. (Chou et al., 2011) Another set of CD34+ MNCs were isolated from the healthy mother and her children who have the *EPAS1* M535V mutation in a five-generation pedigree family (Dr. Prchal, University of Utah Hospital). The CD34+ MNCs were expanded and reprogrammed to hiPSCs using CytoTune-iPS Sendai Reprogramming (Thermofisher, reprogramming carried out by personnel at Cellular Translational Research Core, University of Utah School of Medicine) (CTRC). Characterization of the newly reprogrammed hiPSCs includes 1. G-banding karyotyping at Johns Hopkins Oncology Core; molecular karyotyping using nanostring technologies, at CTRC; 2. Pluripotency markers; and 3. Differentiation potential using embryoid body and teratoma assays (JHU) and STEMdiff Trilineage differentiation assay (Stem Cell Technologies; at CTRC). All hiPSC lines were cultured and maintained with Stemflex medium (Gibco) at passages younger than passage 15 and with E8 medium after passage 20 (Gibco) on vitronectin.(Chen et al., 2011) hiPSCs were collected through digestion with ethylenediaminetetraacetic acid (EDTA; Promega, Madison, WI) and plated at a concentration of $3x10^4$ cells/cm$^2$ with the addition of 10μM ROCK inhibitor, Y27632.

**EC differentiation from hiPSCs**

To initiate mesodermal induction, Essential 6 medium (Gibco) supplemented with 6 μM CHIR-99021 (STEMCELL Technologies) was added to one well of hiPSCs at 70% confluence. (Lian et al., 2014) In early vascular differentiation, cells were plated onto collagen IV (Corning) coated plates at $2x10^4$ cells/cm$^2$ with ROCK inhibitor and cultured in endothelial cell growth medium (Promocell) supplemented with 50 ng/mL VEGF (R&D) and SB-431542 (Sigma-Aldrich, St. Louis, MO), hereafter called high VEGF media. (Kusuma et al., 2015, Kusuma et al., 2013, Kusuma et

al., 2017, Chan et al., 2015) Early ECs (day 8) were magnetically sorted using VEcad-PE (BD Biosciences) and the MACS sorting system (Miltenyi Biotech) according to the manufacturer's instructions. Sorted ECs were cultured and matured on collagen IV coated plates in high VEGF media.

**Vascular SMC differentiation from hiPSCs**

We followed an established protocol for the derivation of contractile SMCs.(Wanjare et al., 2013a, Wanjare et al., 2013b, Wanjare et al., 2014, Eoh et al., 2017) Briefly, hiPSCs were collected through digestion with TrypLE (Invitrogen), and a 40µm mesh strainer (BD Biosciences, San Jose, CA, USA) was used to separate the cells into individual cell suspensions. hiPSCs were seeded at a concentration of $5 \times 10^4$ cells/cm$^2$ onto plates previously coated with collagen IV (Corning). The hiPSCs were cultured for six days in a differentiation medium composed of alpha-MEM (Invitrogen), 10% FBS (Hyclone), and 0.1 mM β-mercaptoethanol (Invitrogen), with the media changed daily. On day 6, differentiated mesodermal cells were collected and seeded at a concentration of $1.25 \times 10^4$ cells/cm$^2$ in differentiation medium with the addition of 10 ng/mL PDGF-BB (R&D Systems) and 1 ng/mL TGFβ1 (R&D Systems) for 6 additional days (a total of 12 days), with media changed every other day. hiPSC-differentiated SMLCs were then collected and subcultured for 6 days towards mSMLCs, which were and subsequently subcultured and reseeded every 6 days (for a total of 30 days) at a 1:1 split ratio in TGFβ1 supplemented alpha-mem media (Invitrogen) with 0.5%-5% FBS (Hyclone)

**Co-cultures**

Different combinations of WT/HIF2 ECs and SMCs were co-cultured using 12mm Transwell® with 0.4µm Pore Polyester Membrane Insert (Corning). Briefly, SMCs were seeded in 12-well wells (22.1mm) at a concentration of $1.25x10^4$/cm$^2$ and ECs were seeded in transwells at a concentration of $1.50 \times 10^4$/cm$^2$ and cultured separately in their respective complete media for 48 hours until confluency. Then, transwells seeded with ECs were moved on top of the SMCs seeded on 12-well wells, and cultured in DMEM+3% FBS for 36 hours. Afterward, cells were collected for RNA. This created a co-culture model in which the ECs and SMCs shared the same conditioned media with each other.(Fillinger et al., 1997)

**Flow cytometry**

Both EC and SMC differentiation were verified using flow cytometry. (Kusuma et al., 2013, Chan et al., 2015) Cells from differentiation were dissociated using TrypLE (Invitrogen). After collection, cells were incubated in the refrigerator for 30 minutes with either FITC- or PE-conjugated antigen-specific antibodies (BD Biosciences; See Supplementary Table 1), in 100 µl (per $2.0 \times 10^6$ cells) of 0.1% bovine serum albumin (BSA; Sigma). After staining, cells were washed three times with 0.1% BSA and passed through a 40 µm strainer (BD) to obtain a single-cell suspension. All analysis was performed with the corresponding isotype as "no stain" controls. Forward-side scatter plots were used to exclude dead cells. User guide instructions were followed to complete the flow cytometry analysis via CellQuest Pro software (BD Biosciences).

**2D immunofluorescent imaging**

Cells were fixed using 3.7% formaldehyde for 5 min at room temperature and washed three times using PBS. The fixed cells were permeabilized in 0.1% Triton-X 100 for 20 min and incubated with 1% BSA blocking solution at room temperature for 30 minutes. (Kusuma et al., 2013, Chan et al., 2015) Samples were incubated with either the antigen-specific primary antibodies for the markers outlined in the text, followed by an appropriate secondary antibodies (Supplementary Table 1), or with phalloidin (1:1000; Molecular Probes) and DAPI (1:10,000; Molecular Probes). Both primary and secondary antibodies were diluted in antibody diluent (DAKO). The immunoconjugated cells were examined using a fluorescent microscope (Zeiss) and imaged

using a confocal microscope (Zeiss LSM 780).

**Quantitative reverse transcriptase PCR**

Total RNA was isolated from cells using TRIzol (Invitrogen) according to the manufacturer's instructions.(Kusuma et al., 2014) Extracted total RNA was quantified using an ultraviolet spectrophotometer and validated for having no DNA contamination. RNA was transcribed using reverse transcriptase M-MLV and oligo(dT) primers (both Promega, Madison, WI). The TaqMan PCR step was performed using TaqMan Universal PCR MasterMix and Gene Expression Assay (Applied Biosystems, Foster City, CA) for genes outlined in the text. The PCR step was performed with a StepOne Real-Time PCR system (Applied Biosystems) according to the manufacturer's instructions. The relative expressions of these genes were normalized to the *GAPDH* amount in the same sample by using the manufacturer's ΔΔCTmethod. For each primer set, the comparative method was used to calculate the amplification differences between different samples. Significance was calculated using unpaired t-test of GraphPad Prism software. Data are represented as mean of 3 to 5 independent experiments ± standard deviation (SD). ***=p<0.001, **=p<0.01 and *=p<0.05.

**Western blot**

Cell lysates were prepared in RIPA buffer (ThermoFisher Scientific) with 1× Protease and Phosphatase Inhibitor Cocktail (ThermoFisher Scientific, MA). Protein isolated from cell lysates was quantified with the BCA assay (ThermoFisher Scientific) and boiled at 95 °C for 5 min in sample buffer and reducing agent. Protein (40µg per well) was loaded into a 4-12% Bis-Tris Protein Gel (ThermoFisher Scientific). Proteins were transferred to nitrocellulose membranes via dry transfer using iBlot2 (ThermoFisher Scientific), blocked in 3 % nonfat milk for 1 h, and incubated overnight at 4 °C (under constant shaking) with respective primary antibody (Supplementary Table 1). Membranes were washed 6 times in Tris-buffered saline containing 0.1% Tween 20 (TBST) for 15 min each and incubated with secondary antibody and anti-GAPDH endogenous control (Supplementary Table 1). Membranes were washed three times in TBST, developed with enhanced chemiluminescence (Pierce) and visualized using the ChemiDoc XRS+ System (Bio-Rad).

**F-actin fiber analysis (ImageJ)**

Grayscale images of WT- or HIF2-SMC phalloidin staining were used in the ImageJ analysis, where 20 cells/image from three separate batches of differentiation were randomly chosen for analysis. (Huang and Helmke, 2011) Briefly, a straight-line tool was used to draw a line across the cell nucleus, perpendicular to the direction of the F-actin fibers. The intensity profile of the F-actin intensity was acquired using the Plot Profile function on ImageJ. Average + SD of the intensity profile of each WT-SMC was obtained using Excel and set as the baseline for F-actin fiber intensity. Intensity profiles of HIF2-SMCs were then compared to the baseline intensity to determine the percentage of cells that have a higher intensity than the baseline.

**Acetylated alpha-tubulin analysis**

Grayscale images of WT or HIF2-SMCs (and HIF2-DMSO or HIF2-Bosentan treated SMCs) acetylated alpha-tubulin staining were used in the ImageJ analysis where 20 cells/image from three separate batches of differentiation were randomly chosen for analysis. Briefly, the freehand selections tool was used to draw the cell outline and measure the area, mean gray fluorescence and the integrated density of each selected cells. Corrected total cell fluorescence (CTCF) of individual cells measured was calculated as below:(Burgess et al., 2010)

CTCF = Integrated Intensity – (Cell Area X Mean Fluorescence of Background Readings)

Mean CTCF of all the selected cells is reported in the bar graph as acetylated alpha-tubulin fluorescence intensity.

**ELISA endothelin-1 quantification**

Conditioned media was collected after 24 hours of incubation of hiPSC-ECs or SMCs or co-cultures. The Human Endothelin-1 Quanti-Glo ELISA Kit (R&D Systems) was used to determine the media concentration of EDN1 according to the manufacturer's instructions. Chemiluminescence reading was done using the SpectraMax i3X microplate reader.

**Atomic force microscopy (AFM)**

An atomic force microscope (MFP-1D; Asylum Research, Goleta, CA, and BioScope Catalyst; Bruker Corporation, Billerica, MA) was used to measure the intrinsic mechanical properties of the hiPSC-SMCs and ECs. The cantilever was adjusted to generate a slight force (~1 nN) onto the cell surface before re-approach. For each cell line, approximately 20 cells were chosen for measurement. Within each cell, 4 separate force measurements were taken. Stiffness was then analyzed as in previous studies (Hung et al., Thomas et al., 2013) using the Sneddon model for contact mechanics to calculate the elastic modulus of the cell. The stiffness of each cell was represented as an average of the 4 separate elastic moduli values. We performed these measurements on three independent biological replicates.

**Assessment of contractility with carbachol**

Studies to analyze cellular contraction were performed by analyzing the cells' responsiveness to $10^{-5}$ M of the cholinergic agonist, carbachol (Calbiochem, Darmstadt, Germany). Calcein, a cytoplasm-viable fluorescence dye, was used to visualize the cells and in a series of confocal microscopy time-lapse images. The change in cell area was then calculated by taking the percent difference in the area at the introduction of the drug and the end of the study (at time 20 minutes).

**Small interfering RNA transfection**

iPSC-derived SMCs were transfected with siGENOME SMARTpool human HIF2A, $ET_A$ and $ET_B$, and scramble control (Dharmacon, Lafayette, CO) following the manufacturer's protocol. Cells were seeded on a six-well plate and treated with either 100nM HIF2A siRNA or a combination of $ET_A$ (66nM) and $ET_B$ (33nM) siRNAs depending on the experiments. For HIF2A siRNA-treated cells: at 96-hour post-transfection, total RNA was collected for qPCR analysis, and total protein was collected for the Western Blot of cytoskeleton protein expression. For $ET_A$ and $ET_B$ siRNAs-treated cells: at 96-hour post-transfection, total RNA was collected for qPCR analysis.

**Bosentan treatment**

hiPSC-derived SMCs were passaged onto a 6-well plate or coverslips (for IF) and cultured for 24 hours. For analysis with AFM, cells were passaged onto 60 mm tissue culture dishes. Then, 10μM of Bosentan was added to the cells for a total of 6 days with SMC medium changes every other day. The control group was treated with the same concentration of DMSO. After 6 days in Bosentan treatment, total RNA was collected for qPCR analysis, and coverslips were fixed for IF analysis. Measurements with AFM were performed as described (refer to the AFM method section).

**Animal model**

*Cohort Description:* All animals used in these studies were maintained under protocols approved by the Animal Care and Use Committee at Johns Hopkins University School of Medicine. *Hif2a*$^{G536W/+}$ mice were initially generated by the laboratory of Frank Lee (Tan, 2013). Mating age-matched non-littermate *Hif2a*$^{G536W/+}$ mice generated subsequent *Hif2a*$^{+/+}$ and

*Hif2a*$^{G536W/+}$ mice. PCR on adult tail DNA was used to identify genotype, using primers for G536W. Male and female mice were used in this study. Age- and gender-matched C57BL/6 (Taconic) mice were used for the control group. *Hif2a*$^{G536W/+}$and C57BL/6 mice were each respectively separated into cohorts and aged (8 - 16 weeks). Animals were housed on a 12-h light/dark cycle and were given access to food and water ad libitum. Animals were sacrificed, and tissues were immediately collected for further experiments.

*PV Loops Acquisition and Analysis:* All mice were weighed before this procedure. Pressure-Volume (PV) loop measurements of the right ventricle (RV) were obtained in accordance with previously published methods (Pacher et al., 2008, Bellofiore et al., 2017).

*PV Loops Analysis:* The following parameters were extracted from PV loops and analyzed: maximum right ventricular pressure produced ($RVP_{max}$), right ventricular pressure at the end of systole ($RVP_{es}$), systolic blood pressure (SBP), pulmonary arterial pressure in systole ($P_{as}$), pulmonary arterial pressure in diastole ($P_{ad}$), maximum rate of contraction ($dP/dt_{max}$), maximum rate of relaxation ($dP/dt_{min}$), and preload recruitable stroke work (PRSW).

*SMC Isolation:* PA tissue was harvested from mice as previously (Hori et al., 2017) (Remillard et al., 2002) with minor modifications (Shimoda et al., 2006, Huetsch, 2018). The PA were transected and gently placed into microcentrifugation tubes containing 2 mg/ml collagenase (type 2, Worthington Biochemical, Lakewood, NJ, USA). The tubes were incubated for 30 minutes in a 37°C water bath before centrifugation at 500 rpm for 5 minutes. The supernatant was discarded, and the pellets were resuspended in DMEM containing 20% fetal bovine serum (FBS) before being transferred into a 35-mm dish. All cell culture dishes used for cell isolation were pre-coated with Collagen I for 1 hour and subsequently washed twice with PBS. At this point, the tissue was manually picked up for second digestion. The tissue was placed into microcentrifugation tubes with reduced $Ca^{2+}$ HBSS (20 μm $CaCl_2$) containing collagenase (type 1; 1750 U/ml, Invitrogen), papain (9.5 U/ml), bovine serum albumin (2 mg/ml) and dithiothreitol (DTT, 1mM) at 37°C for 30 minutes. Following digestion, the tubes were centrifuged at 500 rpm for 5 minutes. The supernatant was discarded, and the pellets were resuspended in DMEM containing 5% FBS. The cells were dispersed by gentle trituration with a wide-bore transfer pipette and placed into a second 35-mm dish. The remaining tissue was then manually picked up out of the 35-mm dish and placed into a third 35-mm dish, filled with DMEM containing 20% FBS. The cells in each condition were monitored for confluency, and the media was changed approximately every 48 hours until confluency at P0 was established. AFM and IF were performed between P0-P1.

*Tensile Testing:* Circumferential tensile testing was performed following protocols described previously (Kobayashi et al., 2005, Hori et al., 2017) with minor modifications (Steppan et al., 2014, Fukunishi et al., 2018). The mPA's were harvested and cleaned. The length of each extracted PA was imaged using a microscope set to a magnification of x10. The length was measured using Image J software (National Institutes of Health [NIH], Bethesda, MD, USA). The rings were then mounted onto pins on an electromechanical puller (DMT560; Danish Myo Technology A/S, Aarhus, Denmark). After appropriate system calibration and pin alignment, the pins were separated using an electromotor at a rate of 50 μm/sec to apply radial force onto the specimen until breakage. Displacement and force were continuously recorded. The thickness of the intimal and medial layers (t) and stress-free lumen diameter (Di) of representative samples was measured from paraffin-embedded, H&E sections, imaged at x4 and x10 magnification and quantified using Image J software.

Engineering Stress (S) was calculated by normalizing force (F) to the initial stress-free area of the specimens (S=F/(2t*L)). Engineering strain (λ) was calculated as the ratio of displacement to the initial stress-free diameter. All calculations were done using Excel (Microsoft, Redmond, WA, USA).

*qRT-PCR, Staining and Quantification:* Harvested mPA and (left) lungs were fixed in 4% paraformaldehyde in buffered PBS for histological sectioning and staining. Other (right) harvested lungs were put in TRIzol for RNA isolation followed by qRT-PCR as detailed previously. Hematoxylin and Eosin, Masson's Trichrome, and Verhoeff van Giesson staining was performed by the Johns Hopkins University Oncology Tissue Services and Reference Histology Cores. Imaging was performed with an upright light microscope (Nikon Accuscope 3000, DS-F12). Image analyses were performed using ImageJ (NIH), MatLab (MathWorks), and Python. Quantification of %Collagen, % Elastin, % ECM, Collagen/Elastin ratio, and vessel area from histology was performed as previously described(Elliott et al., 2019).

**Statistics**

For all experiments, "n" denotes technical replicates while "N" represents biological replicates. Unless otherwise indicated analyses were performed in triplicate samples, N is indicated for each experiment throughout the figure legends. Two-tailed t-test or ANOVA were performed to determine significance. All graphs were drawn using GraphPad Prism 6. Significance levels were set at *p<0.05, **p<0.01, and ***p<0.001.

**Supplemental References**


Bellofiore, A., Vanderpool, R., Brewis, M. J., Peacock, A. J. & Chesler, N. C. 2017. A novel single-beat approach to assess right ventricular systolic function. *Journal of Applied Physiology,* 124**,** 283-290.

Burgess, A., Vigneron, S., Brioudes, E., Labbe, J. C., Lorca, T. & Castro, A. 2010. Loss of human Greatwall results in G2 arrest and multiple mitotic defects due to deregulation of the cyclin B-Cdc2/PP2A balance. *Proceedings of the National Academy of Sciences of the United States of America,* 107**,** 12564-12569.

Chan, X. Y., Black, R., Dickerman, K., Federico, J., Levesque, M., Mumm, J. & Gerecht, S. 2015. Three-Dimensional Vascular Network Assembly From Diabetic Patient-Derived Induced Pluripotent Stem Cells. *Arterioscler Thromb Vasc Biol,* 35**,** 2677-85.

Chen, G., Gulbranson, D. R., Hou, Z., Bolin, J. M., Ruotti, V., Probasco, M. D., Smuga-Otto, K., Howden, S. E., Diol, N. R., Propson, N. E., Wagner, R., Lee, G. O., Antosiewicz-Bourget, J., Teng, J. M. & Thomson, J. A. 2011. Chemically defined conditions for human iPSC derivation and culture. *Nat Methods,* 8**,** 424-9.

Chou, B. K., Mali, P., Huang, X., Ye, Z., Dowey, S. N., Resar, L. M., Zou, C., Zhang, Y. A., Tong, J. & Cheng, L. 2011. Efficient human iPS cell derivation by a non-integrating plasmid from blood cells with unique epigenetic and gene expression signatures. *Cell Res,* 21**,** 518-29.

Elliott, M. B., Ginn, B., Fukunishi, T., Bedja, D., Suresh, A., Chen, T., Inoue, T., Dietz, H. C., Santhanam, L., Mao, H.-Q., Hibino, N. & Gerecht, S. 2019. Regenerative and durable small-diameter graft as an arterial conduit. *Proceedings of the National Academy of Sciences,* 116**,** 12710-12719.

Eoh, J. H., Shen, N., Burke, J. A., Hinderer, S., Xia, Z., Schenke-Layland, K. & Gerecht, S. 2017. Enhanced elastin synthesis and maturation in human vascular smooth muscle tissue derived from induced-pluripotent stem cells. *Acta Biomater*.

Fillinger, M. F., Sampson, L. N., Cronenwett, J. L., Powell, R. J. & Wagner, R. J. 1997. Coculture of endothelial cells and smooth muscle cells in bilayer and conditioned media models. *J Surg Res,* 67**,** 169-78.

Fukunishi, D. T., Ong, D. C. S., Lui, D. C., Pitaktong, M. I., Smoot, M. C., Harris, D. J., Gabriele, M. P., Vricella, D. L., Santhanam, D. L., Lu, D. S. & Hibino, D. N. 2018. Formation of neoarteries with optimal remodeling using rapidly degrading textile vascular grafts. *Tissue Engineering Part A,* 0**,** null.
Hori, D., Dunkerly-Eyring, B., Nomura, Y., Biswas, D., Steppan, J., Henao-Mejia, J., Adachi, H., Santhanam, L., Berkowitz, D. E., Steenbergen, C., Flavell, R. A. & Das, S. 2017. miR-181b regulates vascular stiffness age dependently in part by regulating TGF-beta signaling. *PLoS One,* 12**,** e0174108.
Huang, L. & Helmke, B. P. 2011. A Semi-Automatic Method for Image Analysis of Edge Dynamics in Living Cells. *Cell Mol Bioeng,* 4**,** 205-219.
Huetsch, J. C. W., Jamine; Undem, Clark; Lade, Julie; Yun, Xin; Baksh, Syeda; Jiang, Haiyang; Lai, Ning; Shimoda, Larissa A. 2018. Rho kinase and Na+/H+exchanger mediateendothelin-1-induced pulmonary arterial smoothmuscle cell proliferation and migration. *Physiological Reports,* 6**,** 1-10.
Hung, W.-C., Yang, Jessica r., Yankaskas, Christopher l., Wong, Bin s., Wu, P.-H., Pardo-Pastor, C., Serra, Selma a., Chiang, M.-J., Gu, Z., Wirtz, D., Valverde, Miguel a., Yang, Joy t., Zhang, J. & Konstantopoulos, K. Confinement Sensing and Signal Optimization via Piezo1/PKA and Myosin II Pathways. *Cell Reports,* 15**,** 1430-1441.
Kobayashi, M., Inoue, K., Warabi, E., Minami, T. & Kodama, T. 2005. A Simple Method of Isolating Mouse Aortic Endothelial Cells. *Journal of Atherosclerosis and Thrombosis,* 12**,** 138-142.
Kusuma, S., Facklam, A. & Gerecht, S. 2015. Characterizing human pluripotent-stem-cell-derived vascular cells for tissue engineering applications. *Stem Cells Dev,* 24**,** 451-8.
Kusuma, S., Peijnenburg, E., Patel, P. & Gerecht, S. 2014. Low Oxygen Tension Enhances Endothelial Fate of Human Pluripotent Stem Cells. *Arteriosclerosis Thrombosis and Vascular Biology,* 34**,** 913-920.
Kusuma, S., Shen, Y. I., Hanjaya-Putra, D., Mali, P., Cheng, L. & Gerecht, S. 2013. Self-organized vascular networks from human pluripotent stem cells in a synthetic matrix. *Proc Natl Acad Sci U S A,* 110**,** 12601-6.
Kusuma, S., Smith, Q., Facklam, A. & Gerecht, S. 2017. Micropattern size-dependent endothelial differentiation from a human induced pluripotent stem cell line. *J Tissue Eng Regen Med,* 11**,** 855-861.
Lian, X. J., Bao, X. P., Al-Ahmad, A., Liu, J. L., Wu, Y., Dong, W. T., Dunn, K. K., Shusta, E. V. & Palecek, S. P. 2014. Efficient Differentiation of Human Pluripotent Stem Cells to Endothelial Progenitors via Small-Molecule Activation of WNT Signaling. *Stem Cell Reports,* 3**,** 804-816.
Pacher, P., Nagayama, T., Mukhopadhyay, P., Bátkai, S. & Kass, D. A. 2008. Measurement of cardiac function using pressure-volume conductance catheter technique in mice and rats. *Nature protocols,* 3**,** 1422-1434.
Remillard, C. V., Zhang, W.-M., Shimoda, L. A. & Sham, J. S. K. 2002. Physiological properties and functions of Ca2+sparks in rat intrapulmonary arterial smooth muscle cells. *American Journal of Physiology-Lung Cellular and Molecular Physiology,* 283**,** L433-L444.
Shimoda, L. A., Fallon, M., Pisarcik, S., Wang, J. & Semenza, G. L. 2006. HIF-1 regulates hypoxic induction of NHE1 expression and alkalinization of intracellular pH in pulmonary arterial myocytes. *American Journal of Physiology-Lung Cellular and Molecular Physiology,* 291**,** L941-L949.
Steppan, J., Sikka, G., Jandu, S., Barodka, V., Halushka, M. K., Flavahan, N. A., Belkin, A. M., Nyhan, D., Butlin, M., Avolio, A., Berkowitz, D. E. & Santhanam, L. 2014. Exercise, vascular stiffness, and tissue transglutaminase. *J Am Heart Assoc,* 3**,** e000599.
Tan, Q. K., Heddy; Percy, Melanie J.; Pietrofesa, Ralph; Chen, Li; Khurana,Tejvir S.; Christofidou-Solomidou, Melpo; Lappin, Terence R. J.; Lee, Frank S. 2013. Erythrocytosis and Pulmonary Hypertension in a Mouse Model of Human HIF2A Gain of Function Mutation. *Journal of Biological Chemistry***,** 17134-17144.
Thomas, G., Burnham, N. A., Camesano, T. A. & Wen, Q. 2013. Measuring the Mechanical Properties of Living Cells Using Atomic Force Microscopy. *Jove-Journal of Visualized Experiments*.

Wanjare, M., Kuo, F. & Gerecht, S. 2013a. Derivation and maturation of synthetic and contractile vascular smooth muscle cells from human pluripotent stem cells. *Cardiovasc Res,* 97**,** 321-30.
Wanjare, M., Kusuma, S. & Gerecht, S. 2013b. Perivascular cells in blood vessel regeneration. *Biotechnol J,* 8**,** 434-47.
Wanjare, M., Kusuma, S. & Gerecht, S. 2014. Defining differences among perivascular cells derived from human pluripotent stem cells. *Stem Cell Reports,* 2**,** 561-75.